1. Helioseismology and Asteroseismology

1.1. Introduction

Small amplitude oscillations of the Sun with a period of about 5 minutes were discovered by Bob Leighton (prof. physics, Caltech) and collaborators in 1962. The first really accurate and extensive list of Solar mode frequencies was generated by Ken Libbrecht (Caltech faculty) and Bob Woodward from observations made at Big Bear Solar Observatory, which was started by the late astronomy professor Hal Zirin and operated at that time by Caltech.

Following on these pioneering efforts, an international network of telescopes arranged around the earth in latitude so that the Sun never sets was started in about 1996 by the National Solar Observatory (a NSF funded US institution) to observe solar oscillations. The GONG project (Global Oscillation Network Project) is still running today; see their website at gong.nso.edu. In addition there are a number of satellites that have been launched to study these phenomena, including an instrument called GOLF on SOHO (Solar and Heliospheric Observatory) (sohowww.nascom.nasa.gov), a collaboration between NASA and ESA launched in 1995.

These small amplitude waves are very difficult to detect. In the Sun periods range from 3 to 12 min, but the vertical velocity amplitude of a single mode is only $\sim$3 cm/sec. Many modes are present at a given time, and the maximum surface motions have an amplitude of 1 km/sec.

Such periodic oscillations are observed in the Sun taking advantage of our ability to observe the entire surface (or more correctly half of the surface at a given time) of the Sun. Radial velocities measured from studying absorption lines, the equivalent widths of temperature sensitive lines, or high precision photometry over the surface, are measured

on timescales short compared to 3 min, with continuous monitoring over many months or years. The resulting data sets are Fourier transformed to study the modes of oscillation.

A number of satellites with small telescopes were launched about a decade ago to detect such oscillations in nearby stars; this field is called asteroseismology in analogy to helioseismology. These include MOST (Microvariability and Oscillation of Stars), built by Canada and launched in 2003. It has a telescope with diameter 15 cm and observes through a single broad-band filter which covers from 350 to 700 nm. COROT was built by France with several international collaborators. COROT was launched in Dec. 2006, and contains a 23 cm diameter telescope. It can detect a periodic change in brightness at 500 nm (5000 Å) of 1 part in 10^6 for a 6th mag star with a period of a few days. Such sensitivity cannot be achieved from the ground, except for the Sun.

This field exploded with the launch in March 2009 of NASA's Kepler satellite (P.I. W. Borucki of the NASA Ames Research Center at Moffett Field, California) which stared at the same small field on the sky (area: 115 square degrees) for approximately 3 years. Although its primary mission was the detection of exoplanets via transits, and from Kepler data a list of several thousand candidate exoplanets was generated, the mission also yielded light curves of more than 100,000 stars with exquisite precision and time sampling.

2. Uses of Helioseismology

Before delving into the details, we explain why initially helioseismology and now, with Kepler, asteroseismology, are so useful. The frequencies of the modes of solar oscillations can be measured to very high accuracy, at least 1 part in 10^5. This means that tests of fine details of a Solar model can be carried out by comparing the observed mode frequencies with those predicted from the model.

Parameters in the Solar model which can be studied are those which affect the speed of sound $c_s(r)$ or the mode splittings.

These tests probe the characteristics of the Sun well below the surface, one of the few methods, aside from studying Solar neutrinos, of obtaining any information about such deep layers.

Among the parameters that can be probed in this way are: the He content, the heavy element content Z, the depth of the top of the convection zone, and the mixing length for convection. The rotation as a function of depth can be inferred in this way, including in the stellar core, so that differential rotation both at the surface (studied from sunspot motions) and within the outer part of the Sun, can be measured. All these are for the outer layers of the Sun. Some information on the Solar core can also be obtained, in particular the rotation rate and the strength of the magnetic field (if it is large).

Prior to the Kepler satellite, only the lowest modes of pulsation in the brightest stars could be detected. Now, after several years of Kepler data being analyzed, the modal patterns of thousands of stars have become available through detailed analysis of Kepler light curves and are known almost as well as that of the Sun. These data can be used to determine the parameters given in the above paragraph. Other data that can be determined include, for red giants, whether the core is H-burning or He-Burning (i.e. RGB vs AGB) and the strength of the magnetic field (if it is large). (see Fullo, Cantiello, Stello et al, 2015, Science, 350, 423, arXiv:1510.06960). Even more importantly the mass, radius, and age of these stars can be determined with an accuracy significantly better than any other method might yield.

The first of the two tables below illustrates why it is easier to study red giants than dwarfs like the Sun using astroseismology techniques; the amplitude of the variation in both light and radial velocity is much larger than in the Sun (i.e. in low mass main sequence

stars). The second table indicates the incredibly small uncertainties in the fundamental stellar parameters that can be achieved for some bright stars with Kepler data.

The fundamental scaling equations of asteroseismology, described by Kjeldsen & Bedding (1995, Astronomy & Astrophysics, 293, 87), indicating which stellar parameters control the measured asteroseismology parameters, are given below. A value for T_{eff} obtained from the spectral energy distribution of the star, or from an analysis of its absorption lines, is combined with the measurments for ν_{max} and $\Delta\nu$ to derive the mass and radius, hence the density, etc.

$$\nu_{max} \;=\; \nu_{max,\odot}\; \frac{M/M_{\odot}}{(R/R_{\odot})^2\,\sqrt{T_{eff}/T_{eff\odot}}}\; \mu Hz$$

$$\Delta\nu \;=\; \Delta\nu_{\odot}\; \sqrt{\frac{M/M_{\odot}}{(R/R_{\odot})^3}}\; \mu Hz \;=\; \Delta\nu_{\odot}\; \sqrt{\frac{\rho}{\rho_{\odot}}}$$

Table 1. Comparison of Asteroseismology Parameters: Sun vs Red Giants

Parameter	Units	Sun	Red Giant
v_r amplitude	cm/sec	15	500
Light variation (broad optical band)	ratio	4×10^{-6}	3×10^{-4}
$\nu(max)$ (peak of mode distribution)	μHz	330	60

Table 1. Accuracy of Stellar Parameters for Bright Stars Derived From Kepler Data

Parameter	Uncertainty
Radius	1.2%
Density	1.7%
Mass	3.3%
Distance	4.4%
Age	14.0%

asteroseismic determination of stellar parameters is carried out based on the properties of the readily extractable average global parameters $\langle\Delta\nu\rangle$ and $\nu_{\rm max}$. The former quantity is a proxy of the mean stellar density $\bar{\rho}$ (Ulrich 1986), while the latter has been shown to scale with the surface gravity and effective temperature (Brown et al. 1991; Kjeldsen & Bedding 1995; Bedding & Kjeldsen 2003):

$$\left(\frac{\langle\Delta\nu\rangle}{\langle\Delta\nu_{\odot}\rangle}\right)^{2} \simeq \frac{\bar{\rho}}{\bar{\rho}_{\odot}}\,, \tag{11}$$

$$\frac{\nu_{\rm max}}{\nu_{\rm max,\odot}} \simeq \frac{M}{\rm M_{\odot}}\left(\frac{R}{\rm R_{\odot}}\right)^{-2}\left(\frac{T_{\rm eff}}{T_{\rm eff,\odot}}\right)^{-1/2}\,. \tag{12}$$

Here, $\bar{\rho}_{\odot}$ and $T_{\rm eff,\odot}$ correspond to the solar properties. Consequently, $\langle\Delta\nu\rangle$ and $\nu_{\rm max}$ are the basis of the asteroseismic scaling relations

$$\frac{M}{\rm M_{\odot}} \simeq \left(\frac{\nu_{\rm max}}{\nu_{\rm max,\odot}}\right)^{3}\left(\frac{\langle\Delta\nu\rangle}{\langle\Delta\nu_{\odot}\rangle}\right)^{-4}\left(\frac{T_{\rm eff}}{T_{\rm eff,\odot}}\right)^{3/2}\,, \tag{13}$$

$$\frac{R}{\rm R_{\odot}} \simeq \left(\frac{\nu_{\rm max}}{\nu_{\rm max,\odot}}\right)\left(\frac{\langle\Delta\nu\rangle}{\langle\Delta\nu_{\odot}\rangle}\right)^{-2}\left(\frac{T_{\rm eff}}{T_{\rm eff,\odot}}\right)^{1/2}\,, \tag{14}$$

where $\langle\Delta\nu_{\odot}\rangle$ and $\nu_{\rm max,\odot}$ are the solar values as determined by the same method used to analyse the data.

When a determination of $T_{\rm eff}$ is available, equations 13 and 14 provide masses and radii independent of any stellar models (e.g., Stello et al. 2008; Silva Aguirre et al. 2011b). Coupled to evolutionary tracks the asteroseismic scaling relations can also provide an age estimation

Fig. 1.—

2.1. The Speed of Sound in a Uniform Gas

We begin by deriving the speed of pressure waves in a gas whose equilibrium temperature, density and pressure are independent of position. Pressure waves with a frequency within the range that can be detected by human ears are called acoustic or sound waves. Pressure waves represent oscillations in pressure where the oscillation is in the direction of travel of the wave. Waves where the oscillation is perpendicular to the direction of travel of the wave, such as ocean waves, are called gravity waves. These are abbreviated as p and g waves.

Initially the gas has pressure P_0, density ρ_0 at all points, and is assumed to be at rest. To calculate the oscillation, we need three equations. They are:

(I) the gas moves, this changes ρ

(II) the change in density produces a change in pressure

(III) pressure inequalities produce a force which leads to motion of the gas

The equilibrium values are denoted with subscript 0, the perturbed values are denoted with superscripts 1. The equilibrium velocity is 0, so v denotes the motion of the gas due to the perturbation. In this derivation we retain terms which are first order in the perturbation, but ignore higher order perturbation terms as they will be much smaller.

We assume that the period of oscillation is short compared with the time required for heat to be exchanged with the surrounding material, and hence the oscillations are adiabatic. Thus we already know the form of the second equation.

Since we assume an adiabatic process, the second equation is derived from $P \propto \rho^\gamma$. This implies:

$$\frac{dP}{P} \;=\; \frac{\gamma d\rho}{\rho}. \quad (eq.\ II)$$

The form of this equation for the perturbed gas is:

$$\frac{P^1}{P_0} \;=\; \frac{\gamma \rho^1}{\rho_0} \quad (eq.\ IIp).$$

The first equation is the mass continuity equation (ρv = constant). Since the laws of physics apply to the individual fluid particles, we must follow them within the fluid, and use the Lagrangian form for the derivitives, so that

$$\frac{d}{dt} \;=\; \frac{\partial}{\partial t} \;+\; v\frac{\partial}{\partial x},$$

where the partial derivatives refer to changes at a fixed point.

Equation 1 is thus

$$\frac{\partial \rho}{\partial t} \;+\; \frac{\partial(\rho v)}{\partial x} \;=\; 0 \quad (eq.\ I)$$

Equation 1, for the perturbed gas, becomes:

$$\frac{\partial \rho^1}{\partial t} \;+\; \frac{\partial[(\rho_0 + \rho^1)v]}{\partial x} \;=\; 0$$

Eliminating the second order term, equation Ip is:

$$\frac{\partial \rho^1}{\partial t} \;=\; -\,\rho_0\,\frac{\partial v}{\partial x} \quad (eq.\ Ip).$$

Now we need the force equation (equation III). The pressure force per unit volume is $-\partial P/\partial x$. If we denote the external force per unit volume (if present) as $f(ext)$, then Newton's Law states:

$$\rho \frac{dv}{dt} + \frac{\partial P}{\partial x} \;=\; f(ext)$$

This becomes:

$$\frac{\partial v}{\partial t} \;+\; \frac{v \partial v}{\partial x} + \frac{1}{\rho}\frac{\partial P}{\partial x} \;=\; \frac{f}{\rho} \qquad (eq.\ III)$$

.

We set the external force to 0 and perturb the gas, to get

$$\rho_0 \;\frac{\partial v}{\partial t} \;+\; \rho^1 \;\frac{\partial v}{\partial t} \;+\; \frac{\partial P^1}{\partial x} \;=\; 0.$$

We ignore the second term, which is second order, to get:

$$\frac{\partial v}{\partial t} \;=\; -\,\frac{1}{\rho_0}\frac{\partial P^1}{\partial x} \qquad (eq.\ IIIp).$$

We now have the three required equations set up for the perturbed gas. We need to combine them to eliminate variables to end up with an equation for either P^1 or ρ^1. We combine eq. Ip and IIp to get

$$\frac{\partial \rho^1}{\partial t} \;=\; -\;\rho_0\;\frac{\partial v}{\partial x} \;\text{ becomes }\; \frac{1}{\gamma P_0}\frac{\partial P^1}{\partial t} \;=\; -\;\frac{\partial v}{\partial x} \quad (eq.\ Ip + IIp)$$

We now use eq. IIIp and differentiate, to get:

$$\frac{\partial}{\partial x}[\frac{\partial P^1}{\partial x} \ + \ \rho_0 \frac{\partial v}{\partial t}] \ = \ 0.$$

Substituting in from eq. Ip+IIp, we end up with the wave equation:

$$\frac{\partial^2 P^1}{\partial x^2} \ + \ \frac{\rho_0}{\gamma P_0} \frac{\partial^2 P^1}{\partial t^2} \ = \ 0.$$

The solution to this equation is a wave, $Ae^{i(kx-\omega t)}$ whose velocity is the speed of sound, c_s, where

$$c_s^2 \ = \ \frac{\gamma P_0}{\rho_0} \ = \ \frac{\gamma k T_0}{\mu m_H}.$$

Note that c_s is approximately $\gamma/3 \times$ the mean speed of a particle in the gas.

The structure in a star is more complicated as ρ, T, g and c_s are all functions of depth, but the overall scheme is the same, to perturb the gas, keep only the first order terms, and try to find an oscillatory (wave) solution.

The only "easy" cases to solve are constant density stellar models or polytropes.

2.2. Gravity Waves in Stars

Gravity waves occur when the displacement of a parcel of gas is perpendicular to the direction of travel of the wave. In stars, gravity waves propagate horizontally within a layer of fixed r, while pressure waves, discussed above, propagate vertically. The upward bouyancy force per unit mass (recall the discussion of convection) is

$$F \ = \ \frac{g}{\rho}[\Delta\rho - \delta\rho],$$

where $\Delta\rho$ is the difference in bulk atmospheric density while $\delta\rho$ is the same inside the rising gas parcel. If we rewrite F as $F = -N^2\Delta x$, where

$$N^2 \;=\; -\frac{g}{\rho}[\frac{\Delta\rho}{\Delta x} \;-\; \frac{\delta\rho}{\Delta x}]$$

then when N^2 is positive, we have a wave equation with a sinusoidal solution with frequency N. N is called the Brunt–Vaisala frequency.

We can also write N^2 as

$$N^2 \;=\; -g[\frac{\gamma-1}{\gamma}\frac{1}{P}\frac{dP}{dz} \;-\; \frac{1}{T}\frac{dT}{dz}].$$

The propagation of a gravity wave requires that buoyancy oscillations in adjacent elements of the stellar atmosphere be appropriate coordinated. From the above equation, one can show that gravity waves cannot propagate in convection zones.

Thus gravity waves can propagate with frequencies up to N but not in (through) convection zones. Horizontal gravity waves will have angular frequency N. Gravity waves travelling in other directions will be subject to a reduced bouyant force, and hence will have smaller angular frequencies.

3. Radial Pulsations

The simplest case to consider is a radial pulsation. Perturb a star by compresing it slightly (radial displacements only, and unlike convection, all material at a specific layer r_0 moves up or down simultaneously. The star will expand back outward and slightly overshoot its initial structure, and will oscillate in and out.

If the amplitude of this oscillation decreases with time, the star is stable against pulsation. If not, the pulsation/radial oscillation continues.

We can approximately derive the period Π of the fundamental mode. In this case the stellar radius is 1/4 of a cycle, similar to the fundamental oscillation mode for an open pipe. We set $\Pi = 4R_*/c_s$, where c_s is the speed of sound, which is the speed of a pressure oscillation, and $c_s = \sqrt{P\gamma_{ad}/\rho}$. This leads to a period – density relation of the form $\Pi \propto 1/\sqrt{\rho}$, which holds for simple models such as constant density spheres (discussed below) and polytropes, and holds approximately for real stars.

To do this correctly (or at least more correctly) gets very messy fast. We use the Lagrangian variable $m(r)$ as the independent variable. Then for the pressure,

$$P(m,t) \;=\; P_0(m) + P_1(m,t) \;=\; P_0(m)\;(1 + p(m)\;e^{i\omega t}).$$

where

$$p(m)\;e^{i\omega t} \;=\; P_1(m,t)/P_0(m) \quad \text{and} \quad r(m,t) \;=\; r_0(m)\;[1 + x(m)\;e^{i\omega t}]$$

$$\rho(m,t) \;=\; \rho_0(m) + \rho_1(m,t) \;=\; \rho_0\;[1 + d(m)e^{i\omega t}]$$

These are inserted into the equation of motion,

$$\frac{\partial P}{\partial m} \;=\; -\;\frac{GM(r)}{4\pi r^4} \;-\; \frac{\partial^2 r}{\partial r^2}\;[\frac{1}{4\pi r^2}]$$

Note that for hydrostatic equilibrium only the first two terms of the above equation are present. One then obtains, using

$$\frac{\partial r}{\partial m} \;=\; \frac{1}{4\pi r^2 \rho} \;\;\Rightarrow\; r_0 \frac{\partial x}{\partial r_0} \;=\; -\,3x \;-\; d.$$

the resulting equation:

$$\frac{\partial}{m}(P_0 p) \;=\; [4g_0 + r_0\omega^2]\;\frac{x}{4\pi(r_0)^2}.$$

Next one assumes adiabatic pulsation, $P \;=\; \gamma_{ad}\; d$, and sets up a system of perterbation equations and tries to solve them. Even if one keeps only the first order perturbations, as is done above, finding a solution is complex and messy, and we do not pursue the formal mathematical solution for the waves further.

Instead we consider a simpler example, a sphere of constant density. Then $r_0 \;=\; (3m/4\pi\rho_0)^{1/3}$ and $g_0 \;=\; Gm/r_0^2 \;=\; (4\pi/3)\; Gr_0\rho_0$. $P_0(r_0) \;=\; (2\pi/3)\; G\rho_0^2\;[R_0^2 - r_0^2]$ where R_0 is the stellar radius.

The pulsation wave equation then becomes:

$$\frac{d^2x}{d\xi^2} \;+\; [\frac{4}{\xi} \;-\; \frac{2\rho}{(1-\xi^2)}]\;\frac{dx}{d\xi} \;+\; \frac{A}{(1-\xi^2)}\;x \;=\; 0. \qquad \text{(eq.Puls 1)}$$

where $\xi \;=\; r_0/R_0$ and

$$A = [\frac{3\;\omega^2}{2\pi G\rho_0\gamma_{ad}}] \;+\; \frac{2\;(4-3\gamma_{ad})}{\gamma_{ad}}.$$

Now we look for the simplest solution of this wave equation. We note that for $x \;= x_0$, equation Puls 1 requires that $A = 0$, and the oscillation and has an eigenfrequency

$$\omega_0^2 \;=\; \frac{4\pi}{3}\;G\rho_0\;(3\;\gamma_{ad} \;-4).$$

This is the fundamental mode of pulsation. Note that this mode has a period Π $\Pi \ = \ 1/[G \ \rho \ (3 \ \gamma_{ad} - 4)]^{1/2}$,

$$\Pi \ = \ (1/\nu) \ \propto \ 1/[G \ \rho_0 \ (3 \ \gamma_{ad} - 4)]^{1/2}.$$

This is similar, but not quite identical, to our initial guesstimate for the period of the fundamental mode, $\Pi \ \approx \ 1/\sqrt{G \ \gamma_{ad} \ \rho_0}$, derived from the approximation $\Pi \ = \ 4R^*/c_s$, where c_s is the speed of sound.

1.2.1 1-D Oscillations on a String

Both ends are fixed

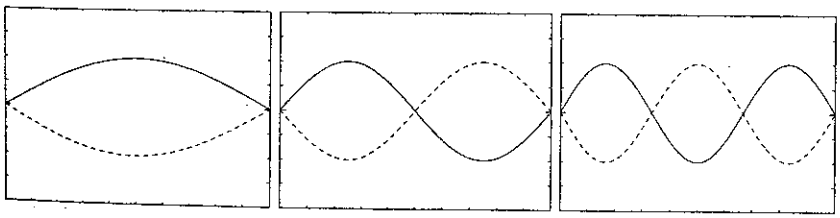

Fig. 1.1. The first three oscillation modes for a string that is fixed at both ends, such as a violin string or a guitar string. On the left is the fundamental mode; in the centre is the first overtone which has a single node; and on the right is the second overtone which has two nodes. Note that the nodes are uniformly spaced.

1.2.2 1-D Oscillations in an Organ Pipe

← this end is open

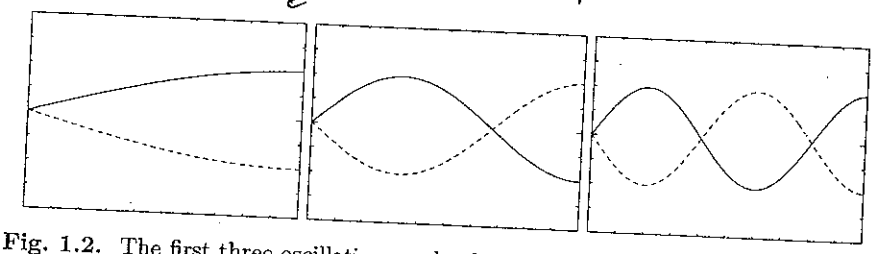

Fig. 1.2. The first three oscillation modes for an organ pipe with one end (on the left) closed, and one end (on the right) open. On the left is the fundamental mode; in the centre is the first overtone which has a single node; and on the right is the second overtone which has two nodes. Note that the open end is an anti-node in the displacement of the air, and that the nodes are uniformly spaced.

From Aerts, Christensen-Dalsgaard, & Kurtz

Asteroseismology (a book published by Springer, 2010)

2D Oscillations (Drum Head)

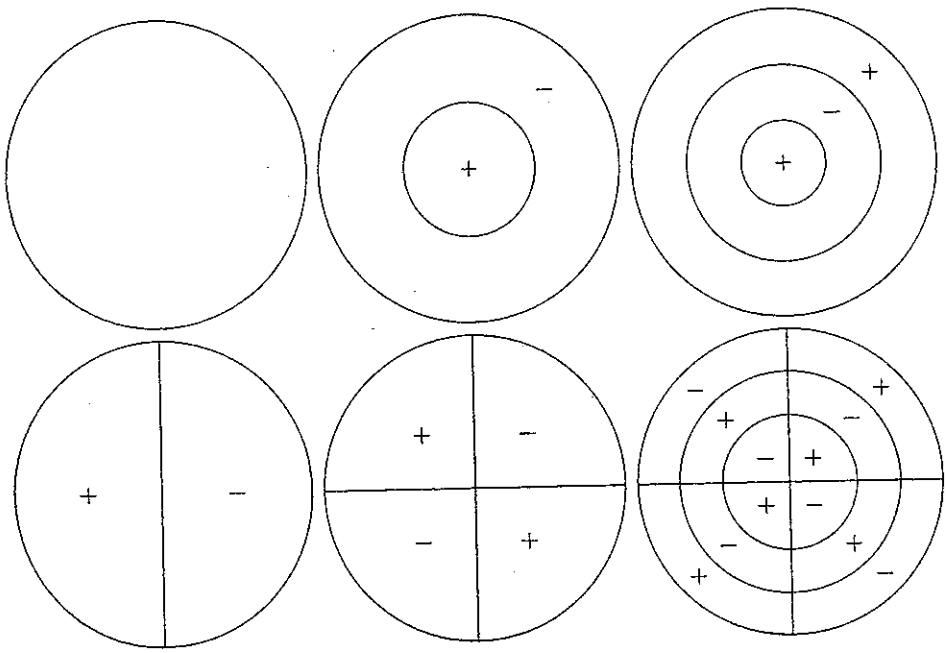

Fig. 1.3. Representations of some oscillation modes in a drum head. The rim of the drum is fixed, so is forced to be a node in all cases. The top left circle represents the fundamental radial mode for the drum: the rim is a node and the centre of the drum is an anti-node. The middle top figure represents the first *radial* overtone, with one node which is a concentric circle. The plus and minus signs indicate that the outer annulus moves outwards while the inner circle moves inwards, and vice versa. The top right figure represents the second radial overtone. The bottom left figure shows the simplest *nonradial* mode for a drum, the dipole mode, where a line across the middle of the drum is a node and one side moves up, while the other moves down, then vice versa. The middle bottom panel represents the quadrupole

Aerts et al

1.4 3-D Oscillations in Stars

Stars are three-dimensional, so their natural oscillation modes have nodes in three orthogonal directions. These are described by the distance r to the centre, co-latitude θ and longitude ϕ; here θ is measured from the pulsation pole, the axis of symmetry (hence is co-latitude, since latitude is measured from the equator). The nodes are concentric shells at constant r, cones of constant θ and planes of constant ϕ. For a spherically symmetric star the solutions to the equations of motion have displacements in the (r, θ, ϕ) directions and are given by[7]

$$\xi_r(r,\theta,\phi,t) = a(r)\, Y_l^m(\theta,\phi) \exp(-\mathrm{i}\, 2\pi\nu t), \tag{1.1}$$

$$\xi_\theta(r,\theta,\phi,t) = b(r) \frac{\partial Y_l^m(\theta,\phi)}{\partial\theta} \exp(-\mathrm{i}\, 2\pi\nu t), \tag{1.2}$$

$$\xi_\phi(r,\theta,\phi,t) = \frac{b(r)}{\sin\theta} \frac{\partial Y_l^m(\theta,\phi)}{\partial\phi} \exp(-\mathrm{i}\, 2\pi\nu t), \tag{1.3}$$

where ξ_r, ξ_θ and ξ_ϕ are the displacements, $a(r)$ and $b(r)$ are amplitudes, ν is the oscillation frequency[8] and $Y_l^m(\theta,\phi)$ are spherical harmonics given by

$$Y_l^m(\theta,\phi) = (-1)^m \sqrt{\frac{2l+1}{4\pi}\frac{(l-m)!}{(l+m)!}} P_l^m(\cos\theta) \exp(\mathrm{i}m\phi) \tag{1.4}$$

and $P_l^m(\cos\theta)$ are Legendre polynomials (see also Appendix B) given by

$$P_l^m(\cos\theta) = \frac{1}{2^l l!}(1-\cos^2\theta)^{m/2} \frac{\mathrm{d}^{l+m}}{\mathrm{d}\cos^{l+m}\theta}(\cos^2\theta - 1)^l. \tag{1.5}$$

Note that the spherical harmonics are usually defined such that the integral of $|Y_l^m|^2$ over the unit sphere equals 1, as secured by the normalization constant

$$c_{lm} \equiv \sqrt{\frac{2l+1}{4\pi}\frac{(l-m)!}{(l+m)!}} \tag{1.6}$$

(*cf.* Eq. (1.4)).

In most pulsating stars the pulsation axis coincides with the rotation axis. The main exceptions are the rapidly oscillating Ap stars where the axis of pulsational symmetry is the magnetic axis which is inclined to the rotational axis (see Section 2.3.5 in Chapter 2).

As with the drum heads, where there were two quantum numbers to specify the modes, for 3-D stars there are three quantum numbers to specify these modes: n is related to the number of radial nodes and is called the *overtone* of the mode[9]; l is the *degree* of the mode and specifies the number of surface nodes that are present; m is the *azimuthal order* of the mode, where $|m|$ specifies how many of the surface nodes are lines of longitude. It follows therefore that the number of surface nodes that are lines of co-latitude is equal to $l - |m|$. The values of m range from $-l$ to $+l$, so there are $2l+1$ modes for each degree l.

Standard spherical harmonics, with factor such that $\oint (Y_l^m)^2 = 1$ sphere

P_l^m Legendre polynomials

Radial modes $l = 0$

Dipole mode $l = 1$ $m = \pm 1, 0$

Quadrupole modes $l = 2$ Aerts et al

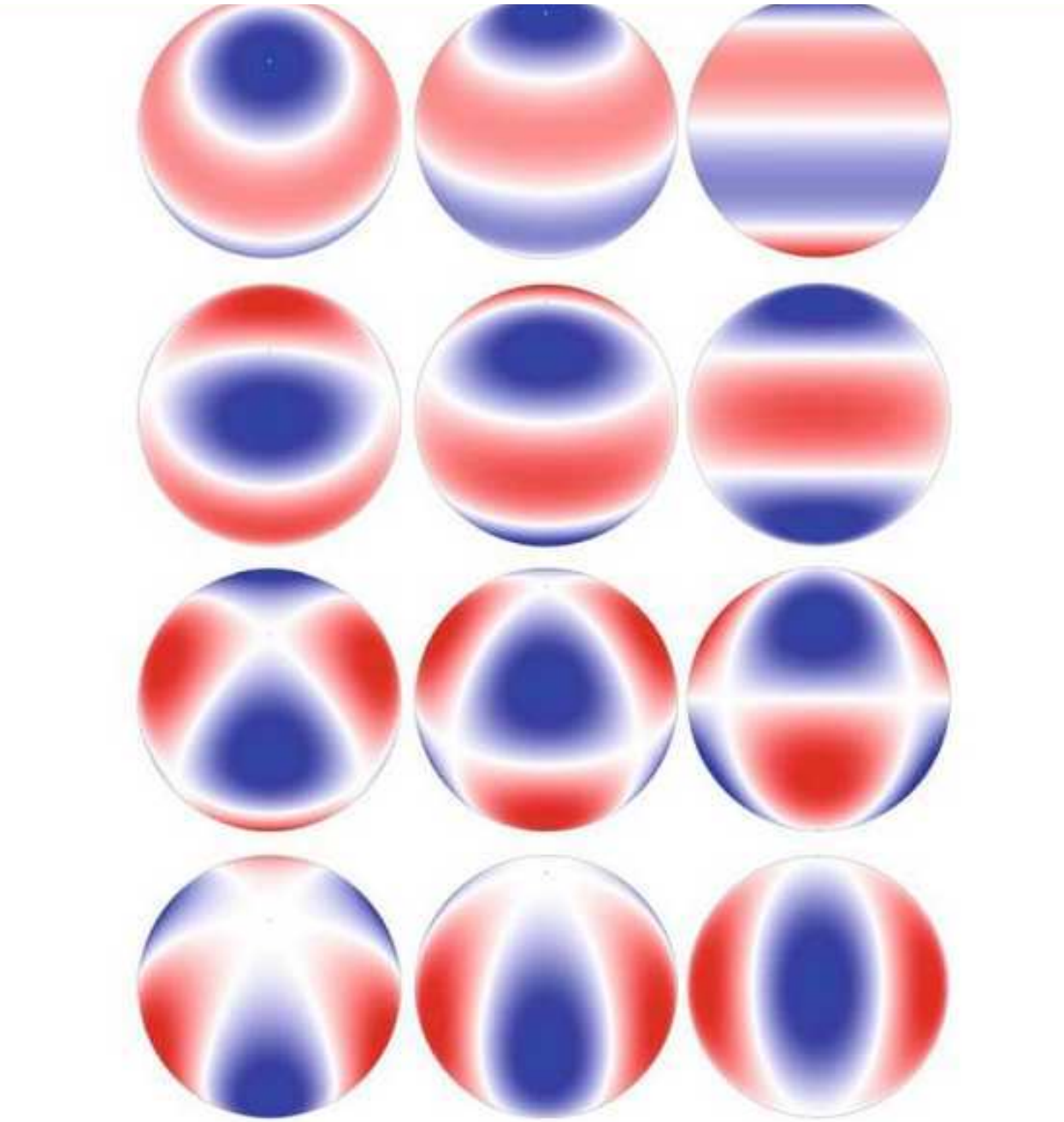

Fig. 1.4. Snapshot of the radial component of the $l = 3$ octupole modes. The columns show the modes from different viewing angles; the left column is for an inclination of the pulsation pole of 30°, the middle column is for 60°, and the right column is for 90°. The white bands represent the positions of the surface nodes; red and blue represent sections of the star that are moving in (out) and/or heating (cooling) at any given time, then vice versa. The top row shows the axisymmetric octupole mode ($l = 3, m = 0$) where the nodes lie at latitudes ±51° and 0°. The second row shows the *tesseral* (meaning $0 < |m| < l$) $l = 3, m = \pm 1$ mode with two nodes that are lines of latitude and one that is a line of longitude. The third row is the tesseral $l = 3, m = \pm 2$ mode, and the bottom row shows the *sectoral* mode (meaning $l = |m|$) with $l = 3, m = \pm 3$. Importantly, rotation distinguishes the sign of m, as discussed in the Section 1.4.3.

3.1. Wave Propagation

Within the Sun the temperature increases rapidly inwards, and thus so does the sound speed, c_s. An average value of c_s for the Sun, adopting $T \sim 6 \times 10^6$ K, is about 4×10^5 m/sec. A pressure wave propagating inwards at an angle from the normal (the radius vector) with velocity $c_s(z)$ will thus be refracted. (Try drawing wave fronts and you will convince yourself of this.) Such a wave, propagating towards higher T (hence higher c_s), will have its lower part in a medium with slightly higher T than the upper part of the wave, and hence will gradually turn around and head back towards the surface of the star where c_s is lower. The shallower the angle with respect to the surface, the smaller the depth the p-wave reaches.

Recall that pressure waves must have angular frequencies $> \omega_c$ where a typical value of $\omega_c \sim c_s/(2H)$ (H is the pressure scale height; $H \sim P_0/(\rho_0 g)$), is $\sim 4 \times 10^{-3}$ radians/sec, corresponding to a maximum period of about 25 minutes for the Sun.

Pressure waves are reflected at the outer surface of the Sun, once the local value of ω_c, which is decreasing toward the surface, reaches ω. A wave with a period of about 3 minutes ($\omega \sim 3.5 \times 10^{-2}$ radians/sec) cannot propagate at heights more than 500 km above the visual solar surface.

Gravity waves can propagate in the interior of the Sun with frequency $N \sim 3 \times 10^{-3}$ sec^{-1} corresponding to a period of $\sim$ 35 minutes. N is the Brunt-Vaisala frequency, which is the angular frequency at which a vertically displaced element will oscillate within a statically stable environment (applicable to ocean waves, atmospheric dynamics, geophysics, asteroseismology, etc). But N goes to 0 when, beginning from deep within the star, the lower boundary of the convection zone is reached, and the interior gravity waves cannot propagate higher than that level. Note that

$$N = \sqrt{-\frac{g}{\rho_0}\frac{\partial\rho(z)}{\partial z}},$$

so gravity waves can only propagate (i.e. there is an oscillatory solution) when $\partial\rho(z)/\partial z$ is negative.

3.2. Waves Inside A Star

We now consider the normal modes of non-radial oscillation of a star. While in principle a pressure or gravity wave can have any ω within the ranges discussed above, in practice only those modes which are resonant will have finite lifetimes.

The center of the star must be a node of any wave which reaches that point as by symmetry the point $r = 0$ cannot be displaced.

The resonant modes are a radial function times the spherical harmonics $Y(l, m)$ with an oscillation term $e^{-i\omega t}$. At first sight the system is spherically symmetric, so that the mode frequency should be a function of n and l only. However, stellar rotation defines an axis which removes this degeneracy and splits the modes such that the p-mode frequency is slightly different for modes of different m. Each mode is split into $2l + 1$ components whose frequencies are separated by the rotational frequency of the star, which on average for the Sun is $\Omega/2\pi \approx 440$ nHz. A star-wide organized magnetic field can also split the modes in this way.

The splitting of the p-modes is given by a large and a small separation. The former is

$$\Delta\nu = (2\int_0^R \frac{dr}{c_s(r)})^{-1}$$

while the small separation is given by

$$\nu_{nl} \;=\; \Delta\nu\;(n + \frac{l}{2}\;+a)\;+\epsilon_{nl},$$

where ϵ_{nl} is a small correction factor and a is a constant whose value is approximately 1.

The splitting of the modes when spherical symmetry is not maintained and the modes depend on m as well is given by

$$\nu_{nlm} \;=\; \nu_{nl0} \;+\; m\;(1 - C_{nl})\;\Omega/(2\pi),$$

where C_{nl} is a constant for the n, l mode which is less than 1.0, and Ω is the rotational velocity of the star.

The radial function for the amplitude of a p-mode satisfies the equation:

$$[\frac{1}{r^2}\frac{d}{dr}(r^2\frac{d}{dr})\;-\;\frac{l(l+1)}{r^2}\;+\;\frac{\omega^2}{c_s^2}]R \;=\; 0.$$

This leads to the identification of the p-modes by their frequency ($\sec^{-1}$) and the horizontal wave number k_h, which indicates the size of 1 wavelength on the solar surface, $k_h = 2\pi/\Delta x$. We set

$$k_h \;=\; \frac{\sqrt{l(l+1)}}{R_\odot},$$

and use l as the degree of oscillation.

The exact solutions of this equation which satisfy the relevant boundary conditions are the eigenvalues of the oscillation problem. For each value of l there are a sequence of modes with radial degree n that have $n-1$ nodes between $r = 0$ and $r = R_\odot$. Eigenfunctions with

low values of l penetrate deep into the Sun, while those with high values of l have very small amplitudes near the center of the Sun.

The turning radius of the mode (r_t) of a pressure wave originating at the surface and propagating downwards, i.e. the radius at which the wave turns to propagate upwards instead, is given in HKT (equation 8.114) as

$$\frac{c_s(r_t)}{r_t} = \frac{2\pi\nu_{nl}}{\sqrt{l(l+1)}},$$

where ν_{nl} is the frequency of the mode. This is due to refraction as indicated earlier.

Movies of solar oscillation modes can be found at several web sites, for example at the website of the BISON project (Birmingham Solar Oscillations Network, a six telescope/six observatory remotely operated solar monitoring array), bison.ph.bham.ac.uk/about/modes.html, or at the Big Bear Solar Observatory web site, www.bbso.njit.edu.

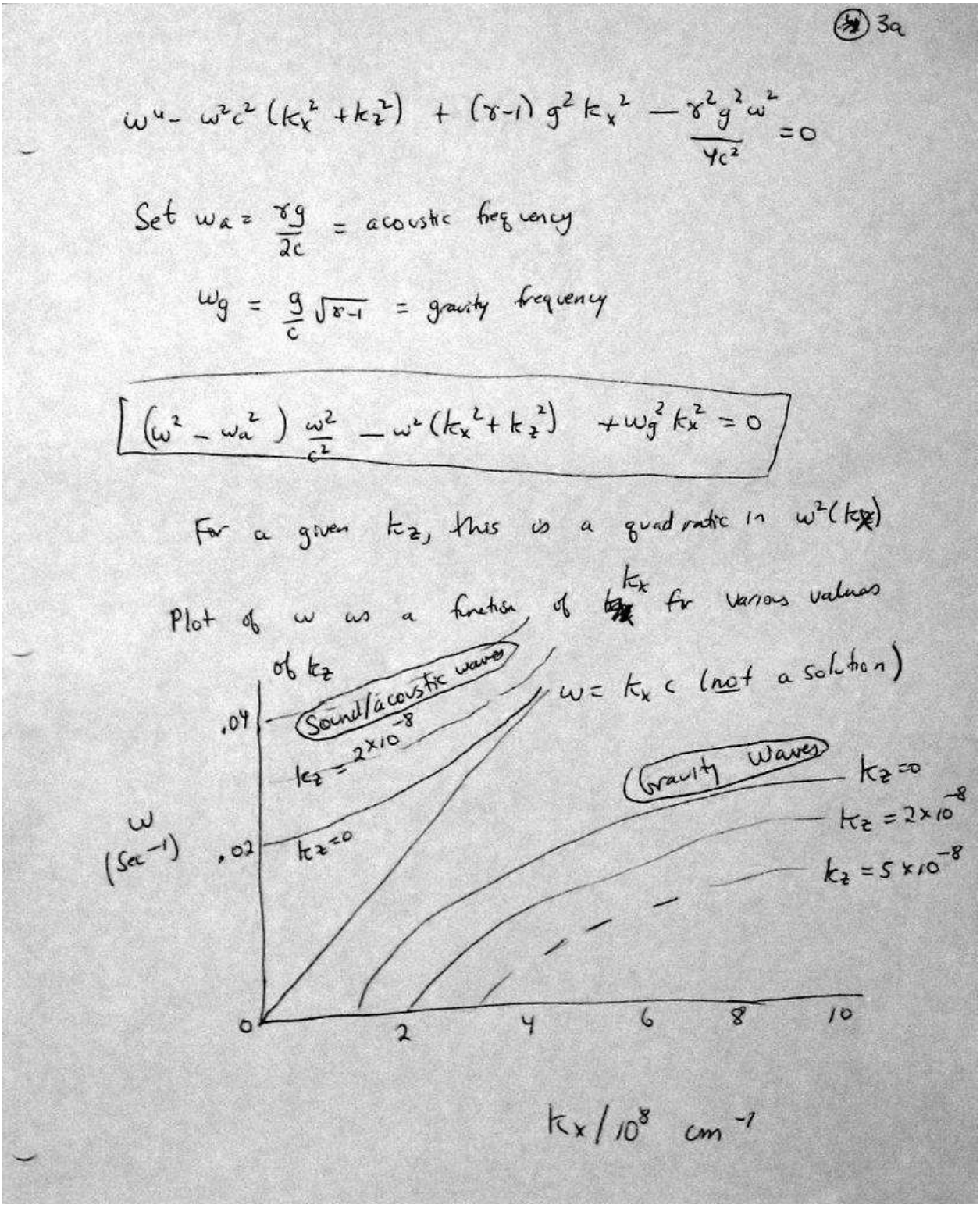

Fig. 2.— Wavenumber versus angular frequency for pressure and gravity waves in the Sun.

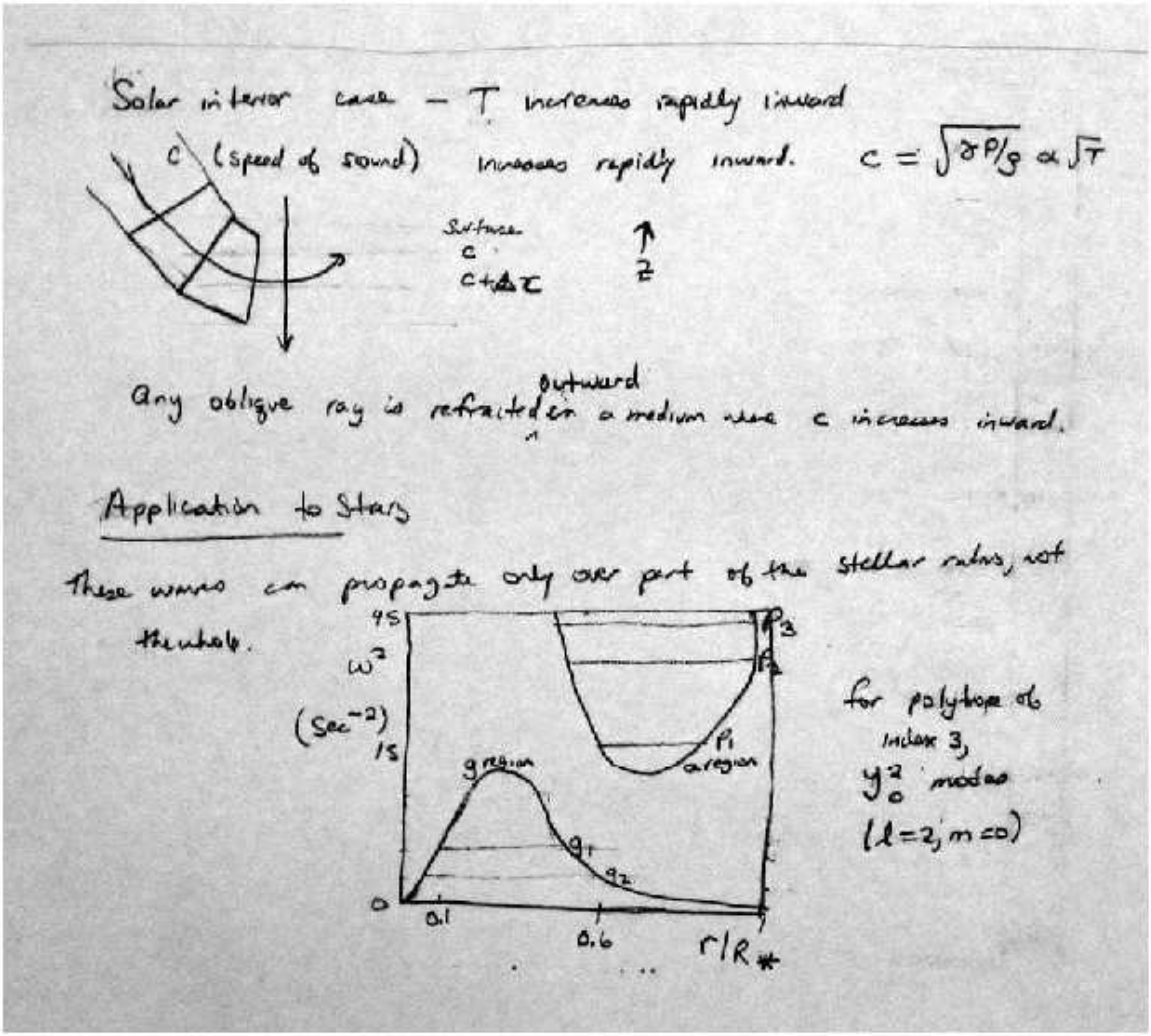

Fig. 3.— Refraction of a pressure wave due to sound speed increasing inward. Sketch of region in radius over which pressure and gravity waves propagate in the Sun.

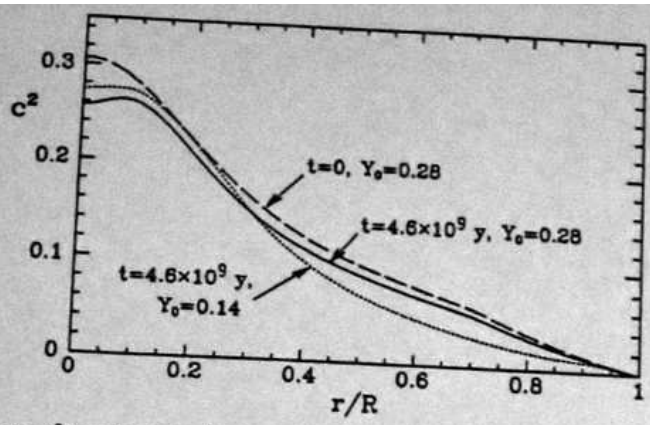

Figure 1 Square of sound speed, c^2, plotted against relative radius r/R in three solar models. The *continuous line* represents a standard model at the current time ($t = 4.6$ Gy) with $Z = 0.02$, $Y_0 = 0.28$; the *dotted line* represents an initially helium-deficient model ($Z = 0.004$, $Y_0 = 0.14$), also at the current time; the *dashed line* represents the model with $Z = 0.02$, $Y_0 = 0.28$ on the zero-age main sequence. The sound speed c is measured in Mm s^{-1}.

GOUGH & TOOMRE

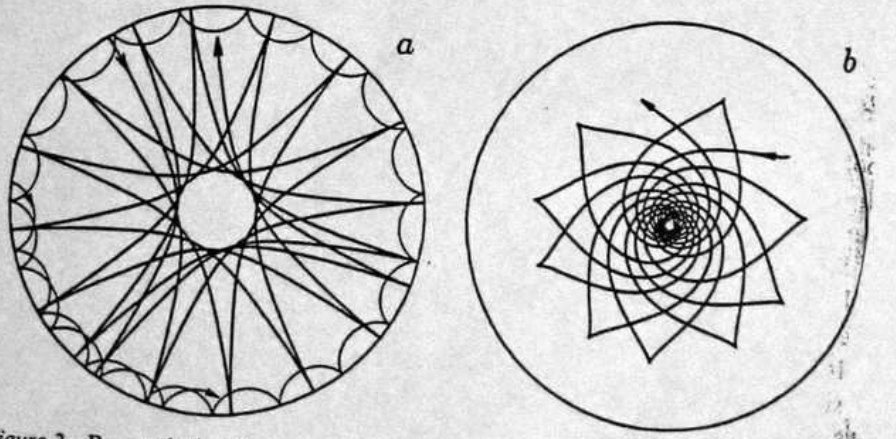

Figure 2 Ray paths in the standard model of the sun represented by the continuous line in Figure 1: (*a*) for two acoustic waves; the more deeply penetrating wave is p_8 ($l = 2$) and the shallower wave is p_8 ($l = 100$); (*b*) for the gravity wave g_{10} ($l = 5$). Note that the number of reflections per revolution is not integral, and indeed is almost never rational, so the ray paths are not closed.

Fig. 5.— Top: Square of sound speed is shown as a function of radius for 3 Solar models. Bottom: ray paths for several pressure and gravity modes.

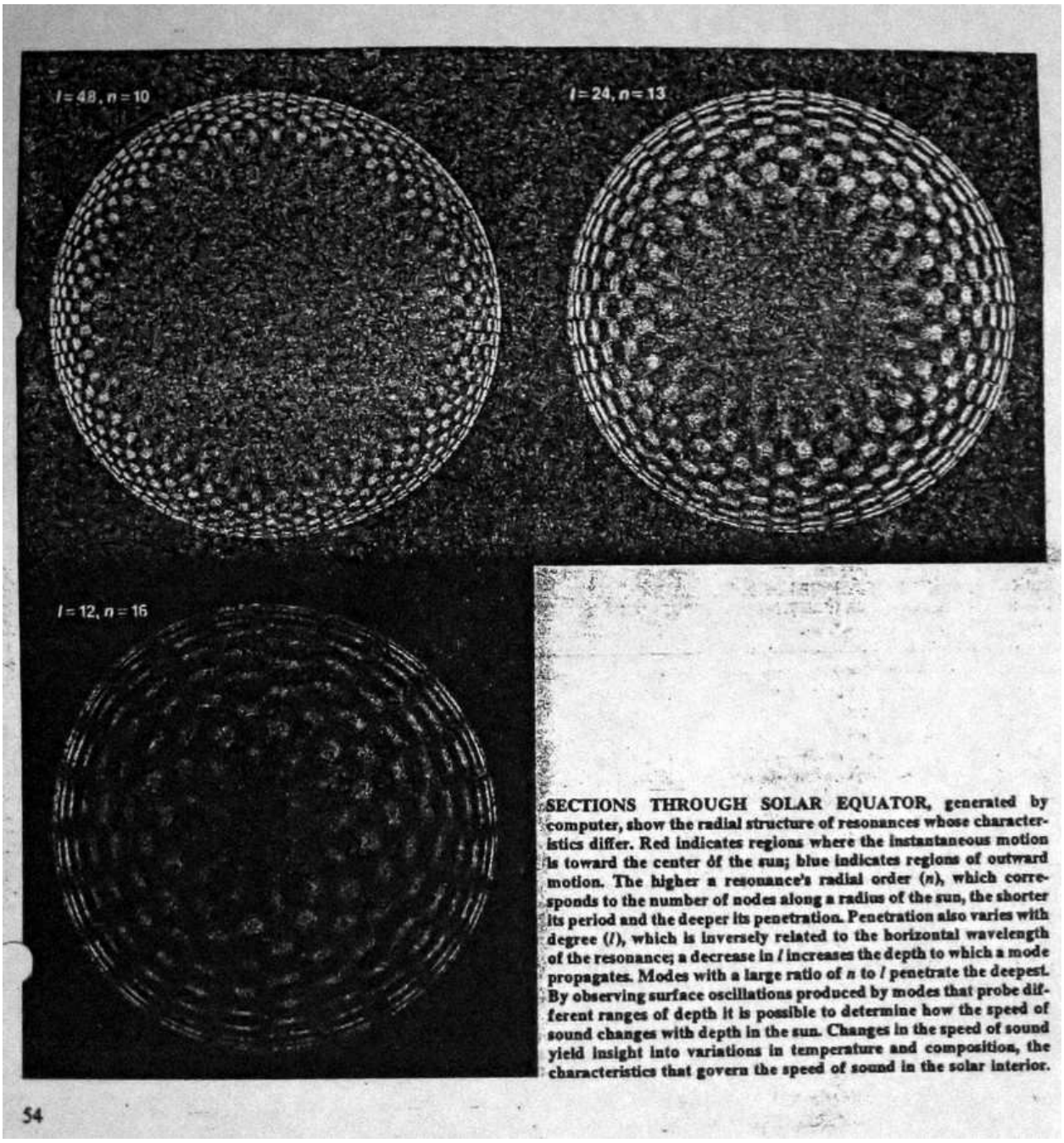

Fig. 6.— Illustration of high order modes.

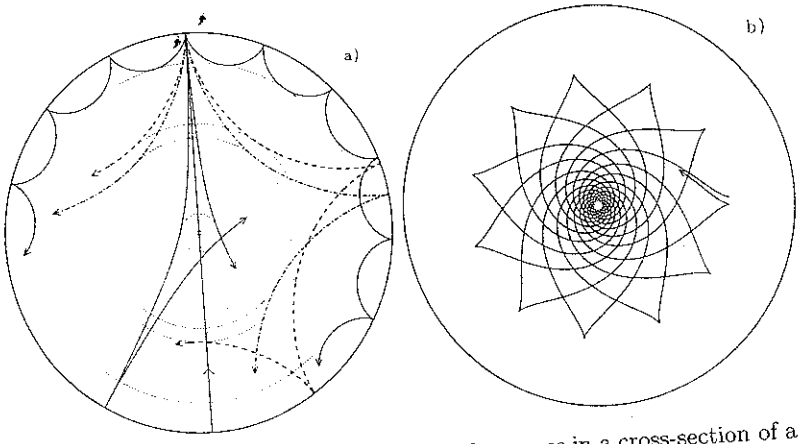

Fig. 1.7. Propagation of rays of sound or gravity waves in a cross-section of a Sun-like star. The acoustic ray paths (panel a) are bend by the increase in sound speed with depth until they reach the inner turning point (indicated by the dotted circles) where they undergo total internal refraction. At the surface the acoustic waves are reflected by the rapid decrease in density. Shown are rays corresponding to modes of frequency 3000 μHz and degrees (in order of increasing penetration depth) $l = 75, 25,$ 20 and 2; the line passing through the centre schematically illustrates the behaviour of a radial mode. The g-mode ray path (panel b) corresponds to a mode of frequency 190 μHz and degree 5 and is trapped in the interior. In this example, it does not propagate in the convective outer part. As we shall see in Chapter 2, g modes are observed at the surface of other types of pulsators. This figure illustrates that the g modes are sensitive to the conditions in the very core of the star, an important property. From Cunha *et al.* (2007).

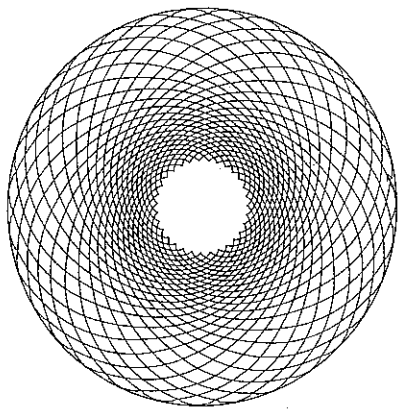

Fig. 1.8. Propagation of rays of gravity waves in a cross-section of an $8\,M_\odot$ ZAMS star. The ray path corresponds to a mode of frequency 50 μHz and degree 5. It is trapped outside the convective core of the star.

Aerts et al

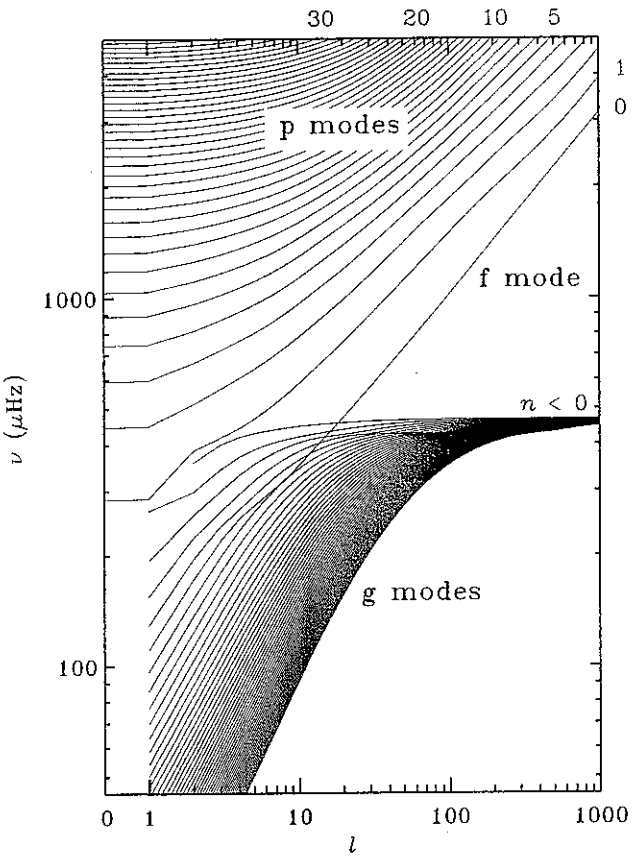

Fig. 1.6. The frequency of modes versus their degree l for a solar model. The figure clearly illustrates the general property of p modes that frequency increases with overtone n and degree l. For g modes frequency decreases with higher overtone, but increases with n if we use the convention that n is negative for g modes. Frequency still increases with degree l for g modes, just as it does for p modes. Some values of the overtone n are given for the p modes lines in the upper right of the figure. Note that while continuous lines are shown for clarity, the individual modes are discrete points, corresponding to integer l, which are not shown here.

Aerts et al

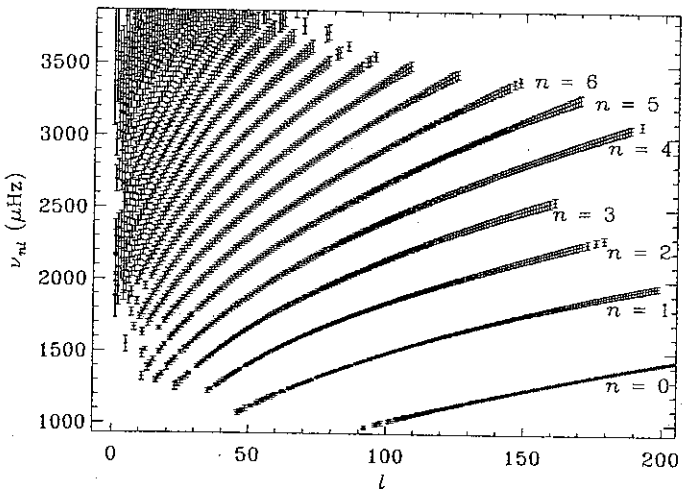

Fig. 7.5. Plot of observed solar p-mode multiplet frequencies, as a function of the degree l, from MDI observations spanning 72 d (Larson & Schou 2008). The vertical lines show the 1000σ error bars. Each ridge corresponds to a given value of the radial order n, which is indicated for the lowest n; note in particular that the lowest ridge corresponds to the f modes, with $n = 0$.

from Aerts et al

The Sun, 72 days of observation

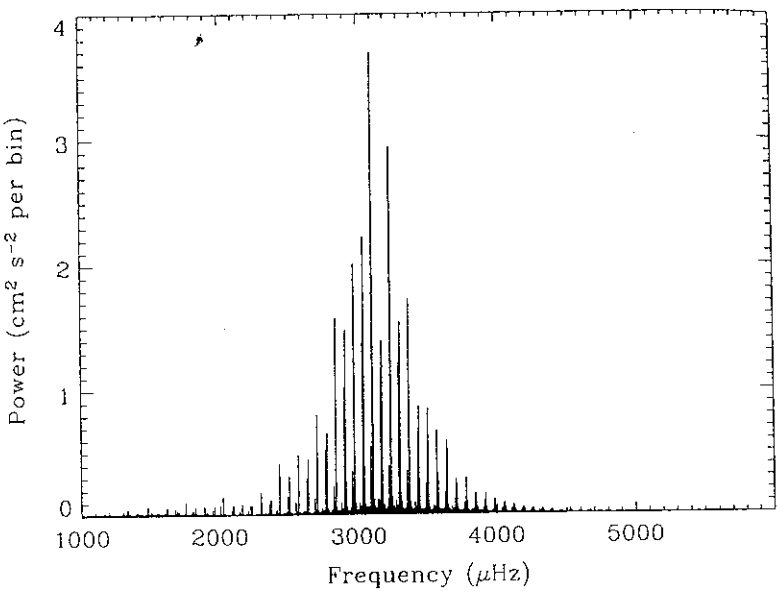

Fig. 1.9. A power spectrum of radial velocity variations in the Sun seen as a star for 9.5 years of data taken with the Birmingham Solar Oscillation Network (BiSON) telescopes. The equivalent amplitude noise level in this diagram is 0.5 mm s^{-1}. Figure courtesy of the BiSON team.

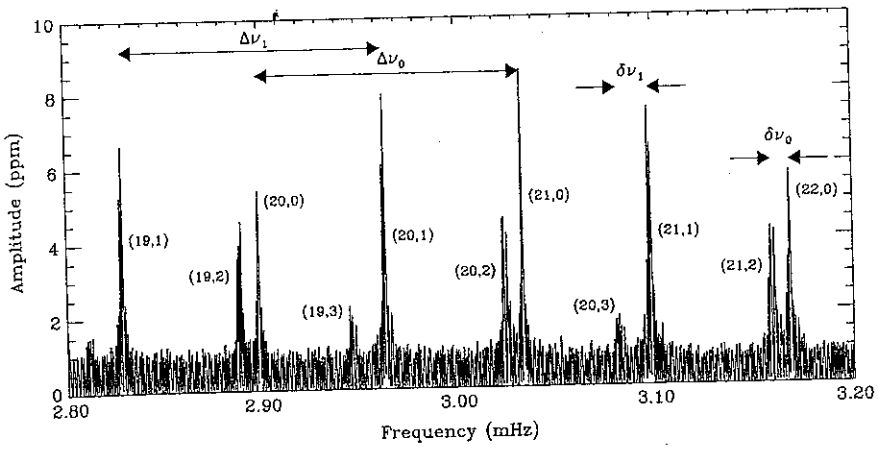

Fig. 1.10. This amplitude spectrum of radial velocity variations observed with the GOLF instrument on SOHO clearly shows the large and small separations in the p modes of the Sun. Courtesy of the GOLF science team.

Aerts et al

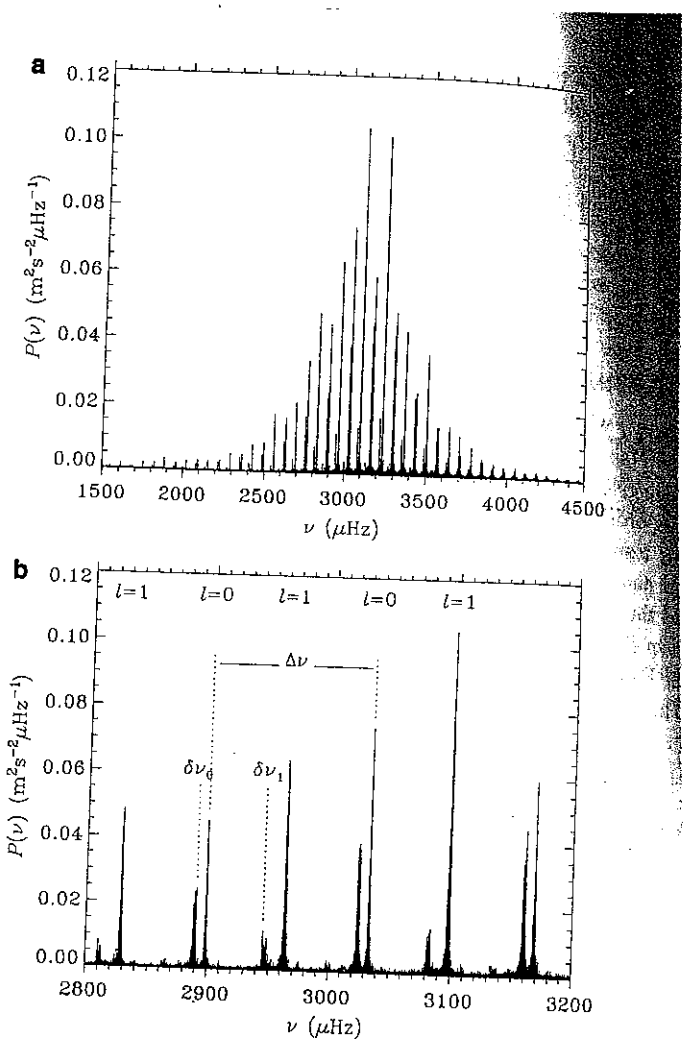

Fig. 7.3. Power spectrum of solar oscillations, obtained from Doppler observations in light integrated over the disc of the Sun. The ordinate is normalized to show velocity power per frequency bin. The data were obtained from the full six-station BiSON network and span approximately 15 yr. Panel (b) provides an expanded view of the central part of the frequency range. Here some modes have been labelled by their degree l, and the large and small frequency separations $\Delta\nu$ and $\delta\nu_l$ have been indicated. See Chaplin *et al.* (2007a).

from Aerts et al

The Sun, 15 years of observation

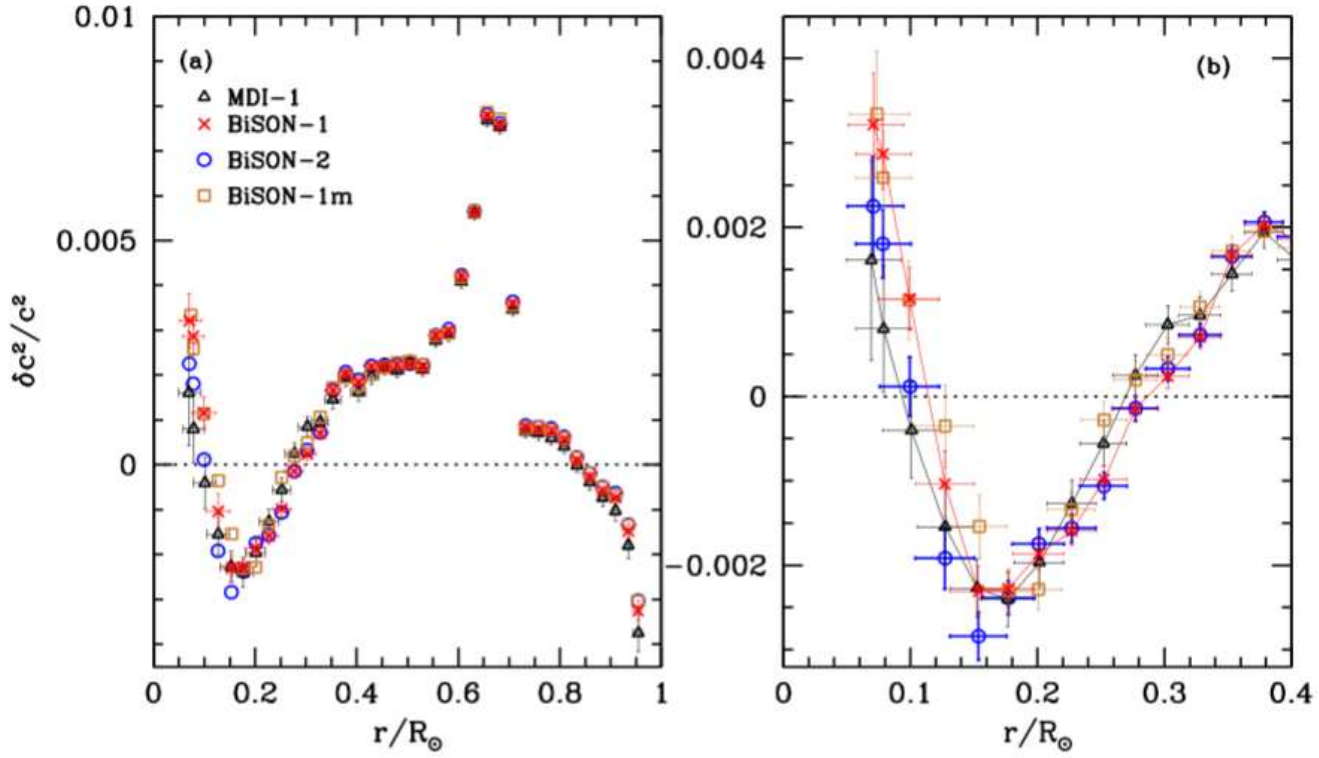

Fig. 3.— The relative difference in the squared sound-speed between the Sun and reference model BP04 obtained by inverting the different data sets marked in the figure. SOLA inversion results are shown. Panel (a) shows the entire radius range, while panel (b) focuses on the core. The vertical error bars are a measure of the errors in the inversion and come from the uncertainties in the frequencies propagated through the inversion process. The horizontal error bars are a measure of the resolution of the inversions, and are the distance distance between the first and third quartile points of the averaging kernels obtained from the inversions. Only two sets of errors are shown in panel (a) for the sale of clarity. In panel (b) we have joined the points corresponding to MDI-1 and BiSON-1 sets to guide the eye.

Fig. 7.— Fig. 3 of Basu, Chaplin, Ellsworth et al, 2009, ApJ, 699, 1403 compares c_s^2 (c_s is the speed of sound) as a function of r of the best solar models with the results from helioseismology. Note the very small vertical scale, i.e. the very good agreement.

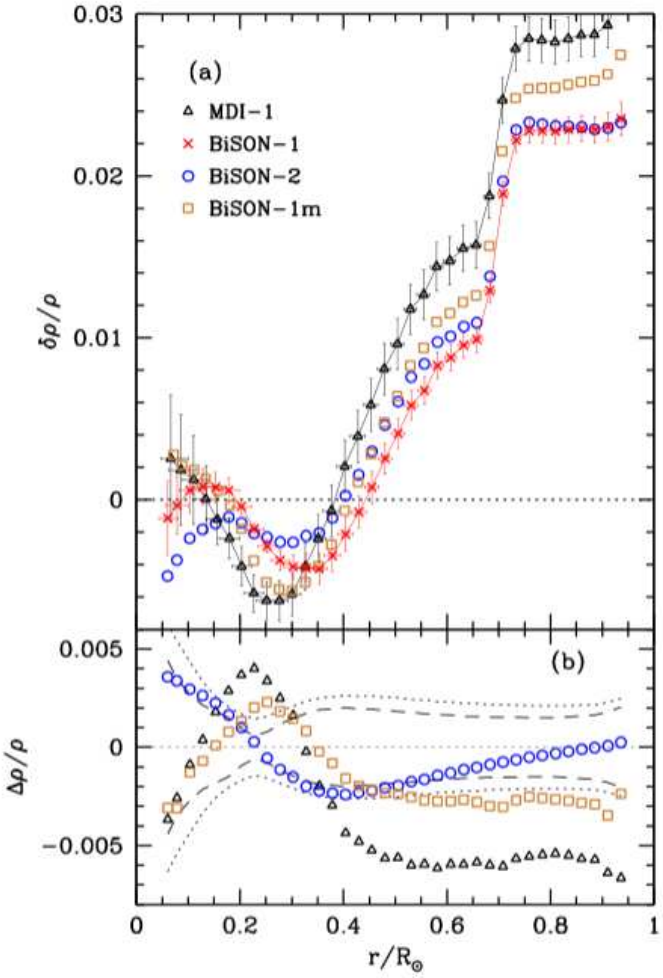

Fig. 8.— Panel (a): Relative density differences between the Sun and reference model BP04 obtained by inverting the data sets marked in the figure. Only two sets of error bars are shown for the sake of clarity. The errors on the other points are similar to those on the BiSON-1 set. Panel (b): The relative differences in the inferred solar density obtained from the different data sets. The differences are taken with respect to the solar density inferred by using the BiSON-1 set. The dotted line shows the 1σ error limit for the MDI-1 set, the dashed line is for the other BiSON sets. Note that there are significant differences in the results. Only SOLA inversion results are shown for the sake of clarity.

Fig. 8.— Fig. 8 of Basu, Chaplin, Ellsworth et al, 2009, ApJ, 699, 1403 compares the density of the best solar model with that inferred from helioseismology. Note the very vertical scale, i.e. the very small differences.

4. Asteroseismology

The first major asteroseismology project was the Whole Earth Telescope set up by Don Winget of the University of Texas at Austin. This was a collaboration of people interested in asteroseismology at several observatories with small telescopes. The mode of operation was that they all joined in targeted photometric campaigns focused on a single star, each of which lasted for several months. They had 1 or two such joint campaigns per year.

Because one cannot resolve the surface of stars other than the Sun (except with interferometry, and there not in any detail), prior to the launch of the Kepler satellite, one could only hope to detect low order modes in other stars. These have been seen in many stars. The photometric precision with ground-based observations is not good enough to detect higher order modes in general. Such higher order modes largely cancel out in the integrated light across the surface of a star. The modes that are of highest amplitude in a particular star may vary with time and are not always the same.

Groups of stars pulsating in non-radial modes include stars similar to the Sun, PG 1159 stars (very hot hydrogen deficient post-AGB stars, with surface layers rich in He, C and O) (Vauclair et al, 2002), ZZ Ceti stars, and pulsating white dwarfs (see the appended HR diagram).

If a star is evolving very rapidly, then one may be able to measure the change in period with time for a particular pulsation mode. This provides a very useful check on stellar evolution and pulsational theory. Such a test has been carried out for a small number of compact stars with short period oscillations as well as for many Cepheid variables. (Cepheids are fundamental mode radial oscillators, a case to be discussed below.)

FIg. 10 shows families of pulsating stars in a T_{eff} vs luminosity HR diagram. Some with evolutionary tracks are superposed. . Hatching from upper right to lower left indicates

g-mode pulsators, while from lower left to upper right denotes p-mode pulsators. The acronyms are usually the name of the first example known, usually a very bright star. DOV are hot white dwarfs; DBV and DAV stars are variable DB (He-rich) an DA (H-rich) white dwarfs. The parallel long-dashed lines in the upper right part of the figure indicate the Cepheid instability strip.

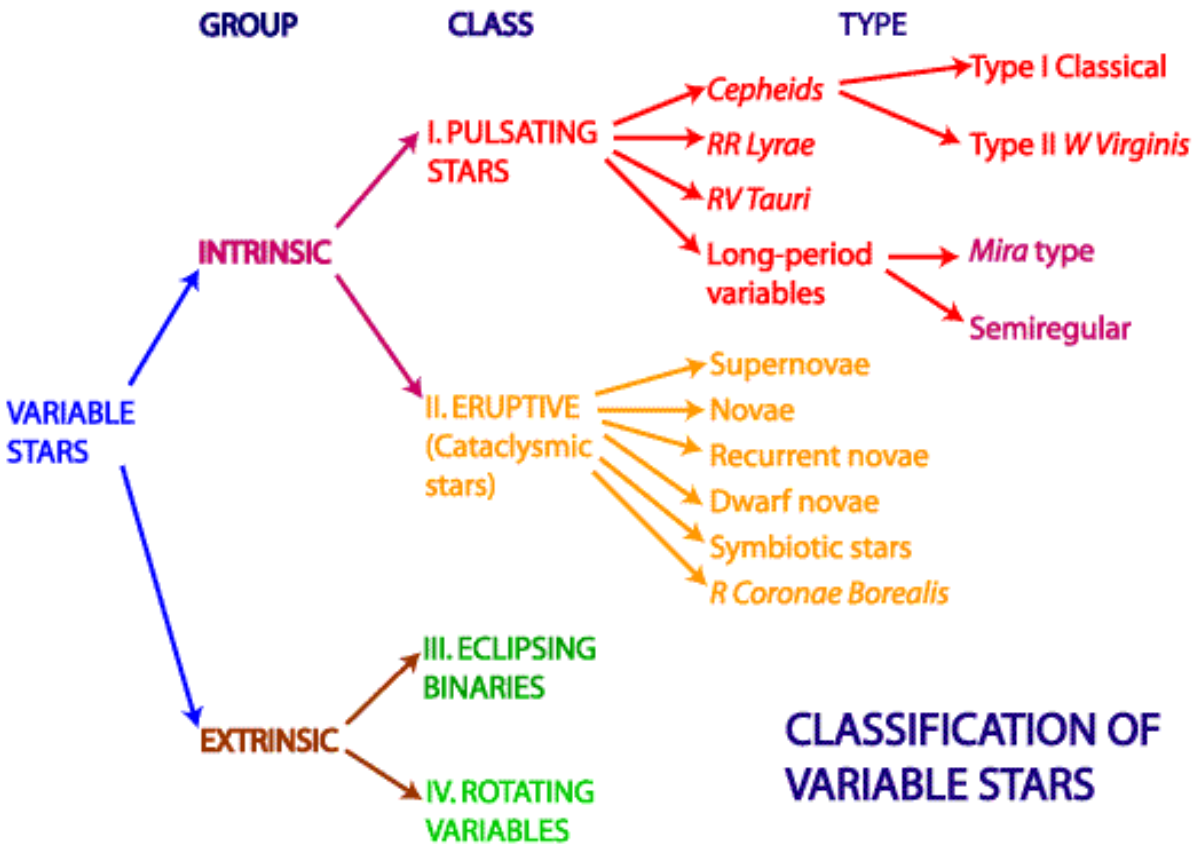
GROUP
CLASS
TYPE
VARIABLE STARS
INTRINSIC
EXTRINSIC
I. PULSATING STARS
II. ERUPTIVE (Cataclysmic stars)
III. ECLIPSING BINARIES
IV. ROTATING VARIABLES
Cepheids
RR Lyrae
RV Tauri
Long-period variables
Type I Classical
Type II W Virginis
Mira type
Semiregular
Supernovae
Novae
Recurrent novae
Dwarf novae
Symbiotic stars
R Coronae Borealis
CLASSIFICATION OF VARIABLE STARS

Fig. 9.—

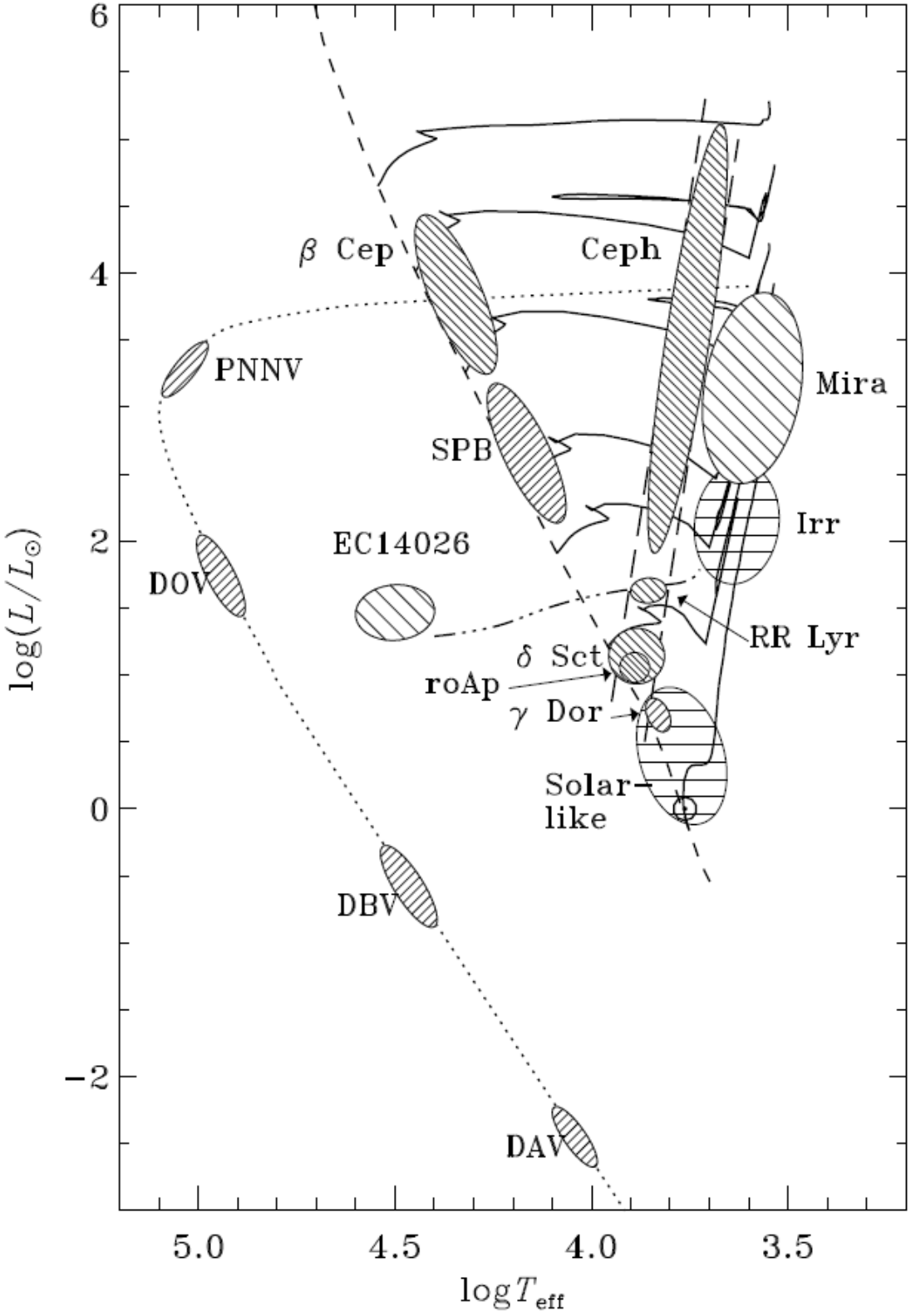

Fig. 10.— The families of pulsating stars are shown. See text on previous page for details. Figure from Christensen-Dalsgaard's online lecture notes.

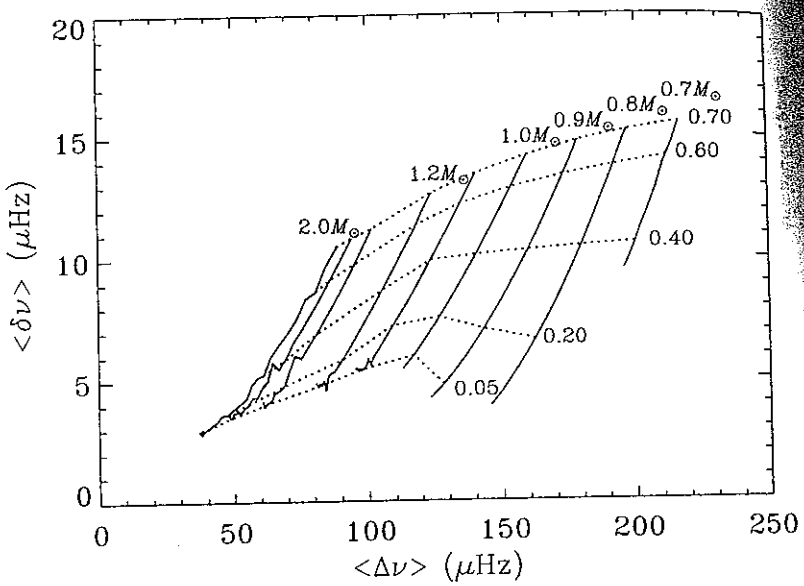

Fig. 1.11. An asteroseismic HR Diagram in which the large separation $\Delta\nu$ is most sensitive to mass, and the small separation $\delta\nu$ is most sensitive to age. The solid, nearly vertical lines are lines of constant mass, and the nearly horizontal dashed lines are isopleths of constant hydrogen mass fraction in the core, at the values indicated in the figure.

Aerts et al

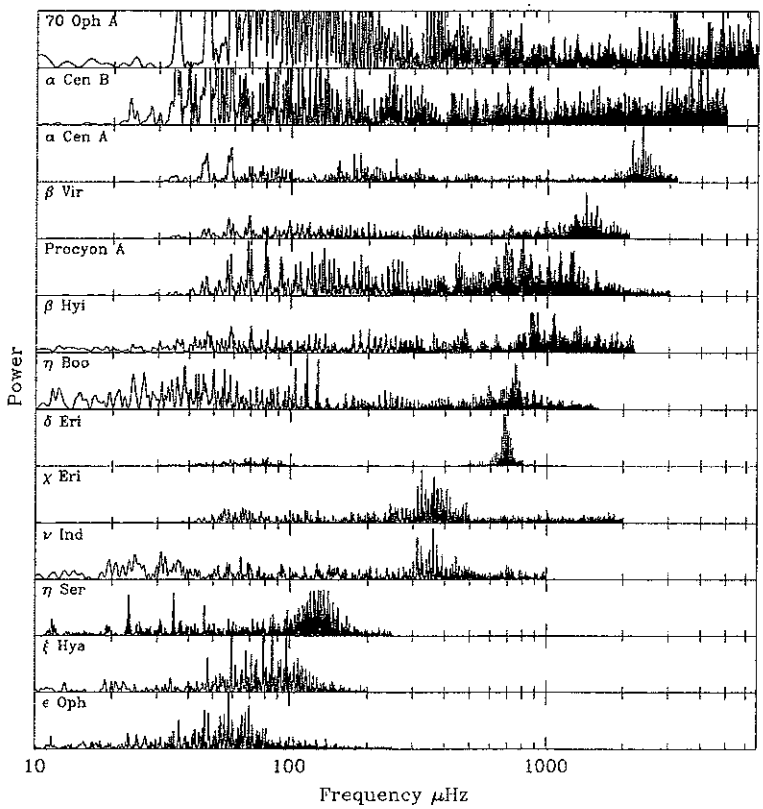

Fig. 2.3. Frequency spectra of a sample of solar-like oscillators covering the entire range in spectral type. Figure courtesy of Fabien Carrier.

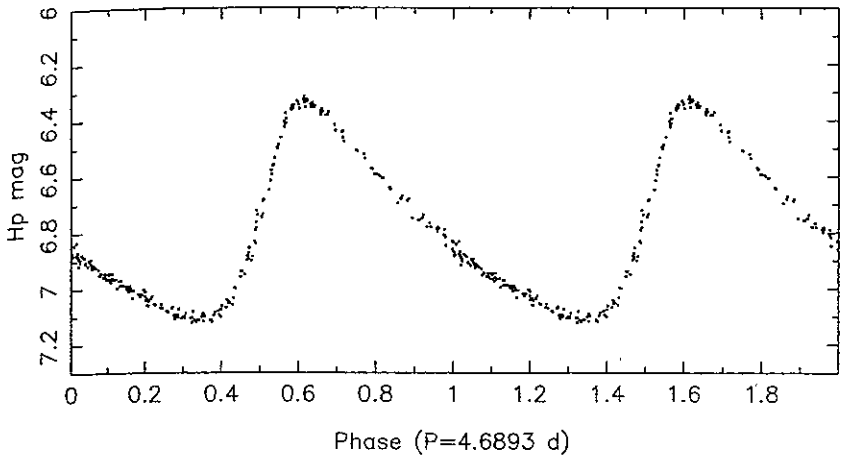

Fig. 2.33. Hipparcos light curve of the classical Cepheid HD 112044 folded according to the oscillation period. Data taken from Perryman (1997, ESA).

Aerts et al.

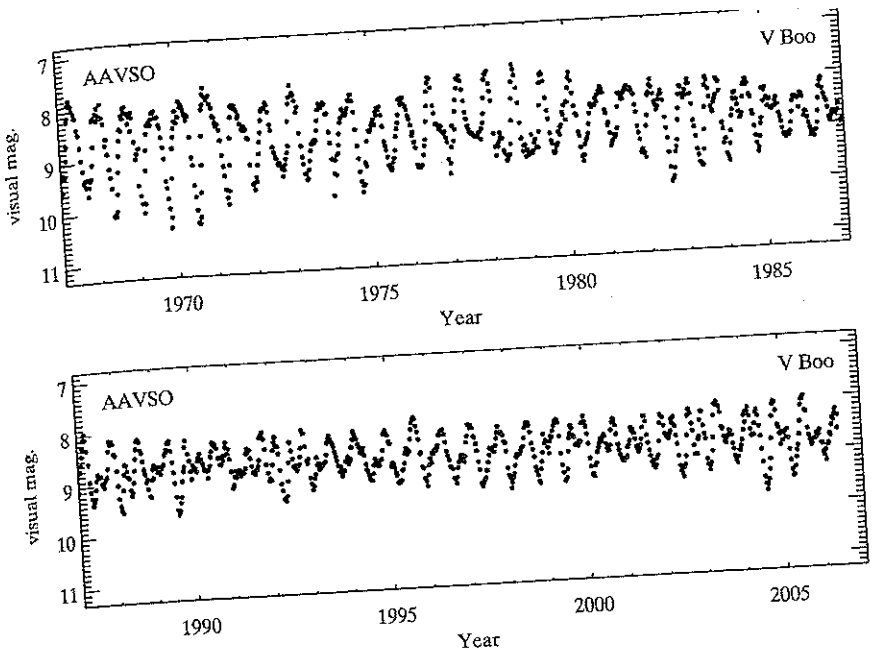

Fig. 2.40. The visual light curve of the SRa star V Boo as observed by amateur astronomers of the AAVSO. Figure courtesy of Matthew Templeton.

Light curve of a ~~Semi-regular~~

Semi-regular long period Variable

(period ≈ 6 months)

Nok X axis is years

AAVSO = American amateur astronomers Variable star observers

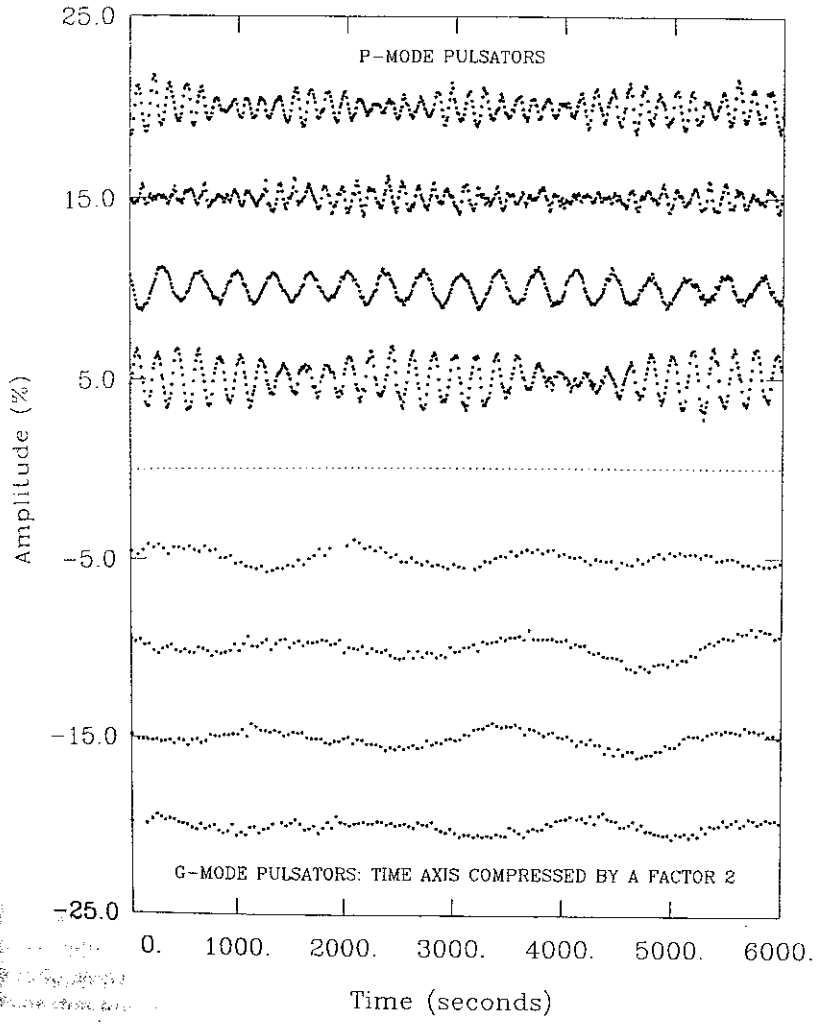

Fig. 2.52. Comparison between the light variations of four sdB p-mode oscillators (upper panel) and four sdB g-mode oscillators (lower panel). The time axis refers to the top half of the figure; the light curves in the bottom half have been compressed by a factor two for visual purposes. From Fontaine *et al.* (2003a).

p mode oscillators
vs
g mode oscillators

Aerts et al

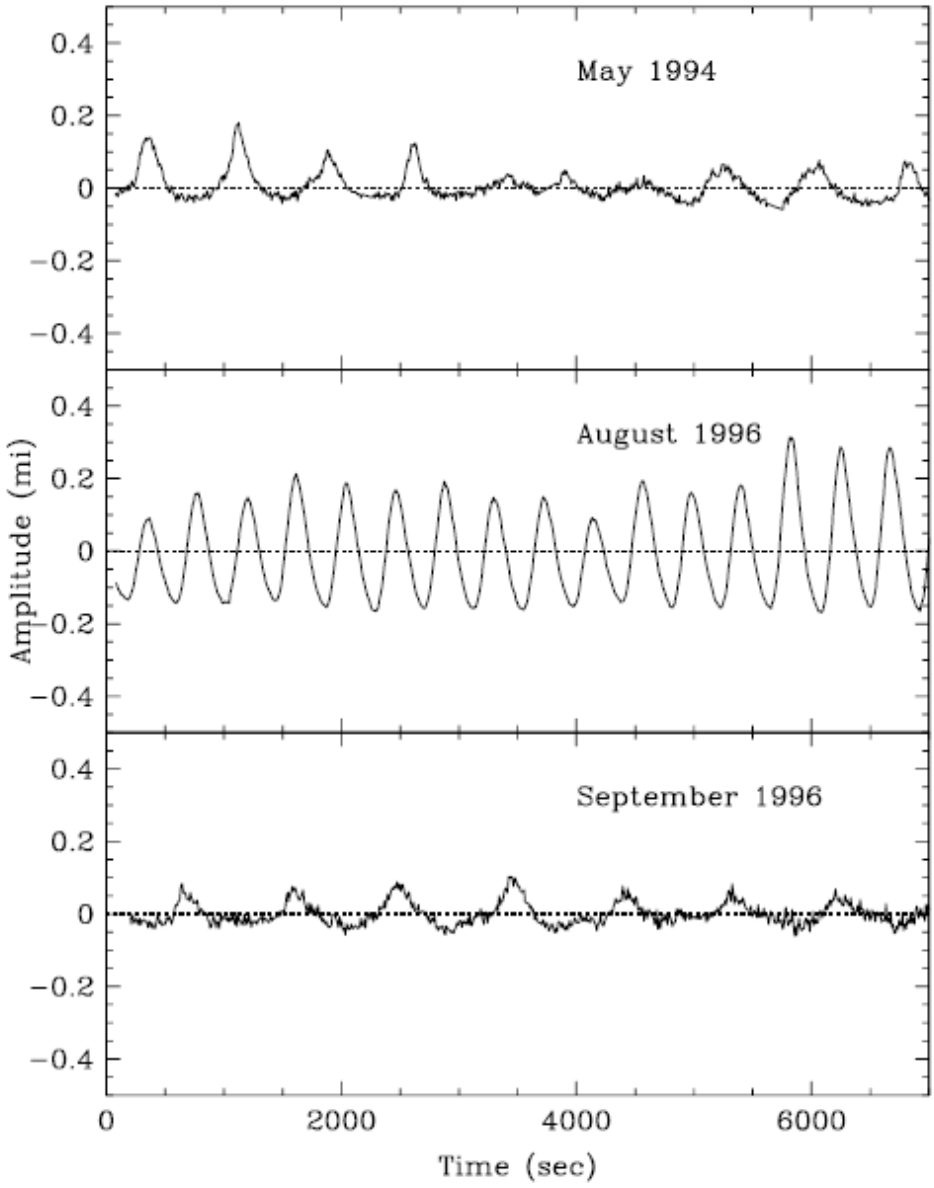

Fig. 8. GD 358 lightcurves over time. The shape of the lightcurve was sinusoidal when the amplitude was highest. The 1994 and September 1996 data exhibit similar pulse shapes and their corresponding power spectra also look similar

Fig. 11.— The light curve of the pulsating white dwarf GD 358 at three different epochs. The vertical scale is mag. (From the WET, Kepler et al. 2003)

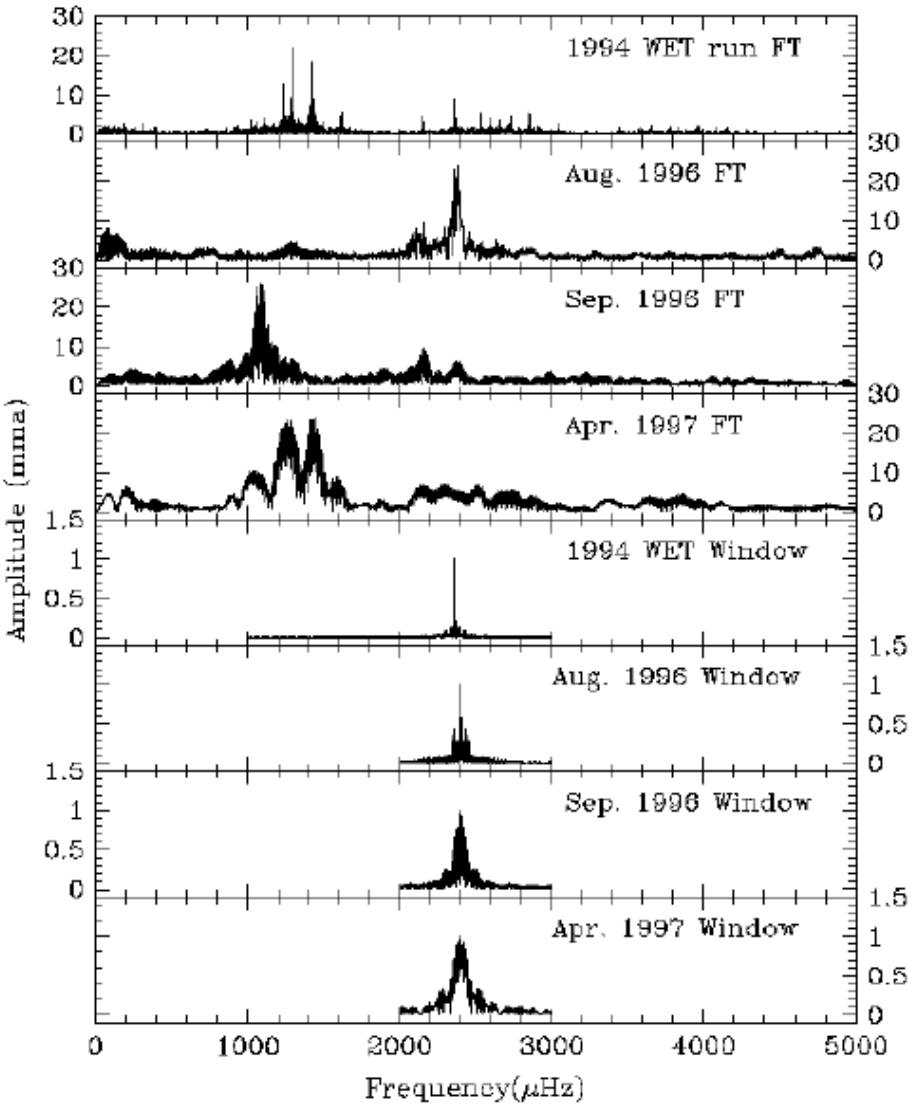

Fig. 7. GD 358 Fourier transform at four different times along with their spectral windows. The 1994 and 1997 Fourier transforms look similar (within the observed frequency resolution, that is). The September 1996 data look similar as well to these two data sets, but the highest amplitude modes have shorter frequencies (longer period). Obviously, the August 1996 Fourier transform looks very different from the other Fourier transforms.

Fig. 12.— The power spectrum for photometry of GD 358 at different epochs. (From the WET, Kepler et al. 2003)

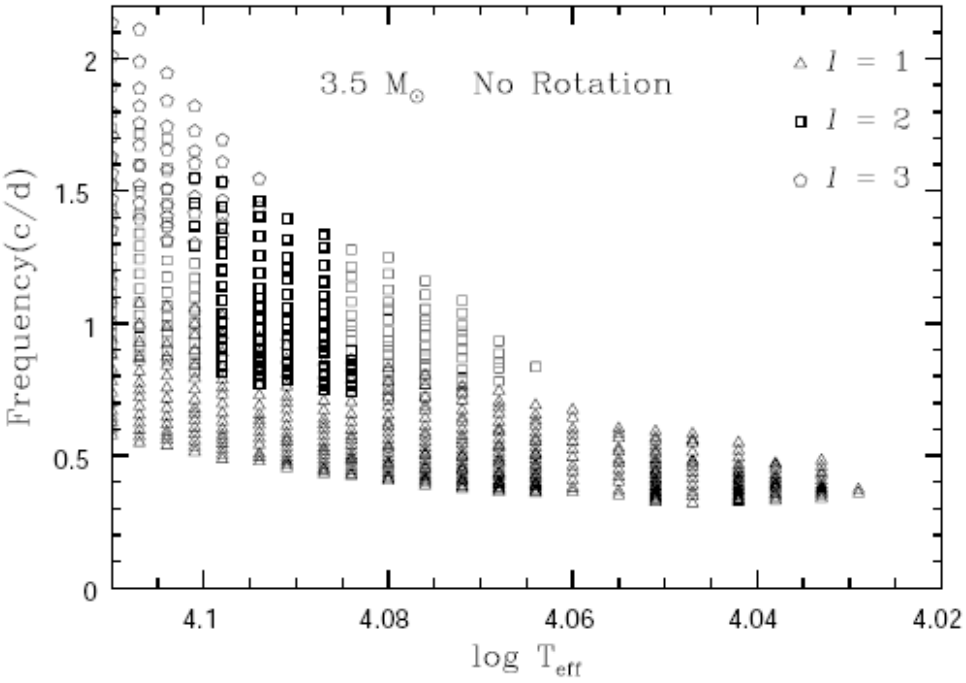

Fig. 4.— Frequencies of g-modes excited in non-rotating models along the $3.5M_{\odot}$ main-sequence evolution. The evolutionary track is shown in Fig. 3.

Fig. 13.— Predicted frequencies (cycles/day) of the g-modes for the late type main sequence Be star β CMi (B8Ve) as it evolves off the main sequence from T_{eff} 12,900 K to 10,500 K. (From Saio, Cameron, Kuschnig et al, 2007)

5. Radial Modes

We now repeat our earlier derivation for eigenfunctions and their frequencies using spherical coordinates to search for the radial modes. We need the same three equations described earlier. We use the same notation as before, so that for example ρ^1 is the (small) change in density as compared to the initial equilibrium value ρ_0. We again assume adiabatic conditions for the moving parcel of gas. Thus equation 2 is the same as before, and is derived from $P \propto \rho^\gamma$. Its perturbed form is also identical to equation IIp given earlier.

Equation 1 (mass conservation) is now

$$\frac{\partial M_r}{\partial r} \;=\; 4\pi r^2 \rho \quad (eq.\ I\ radial)$$

To obtain the perturbed form of this equation, we note that the left side becomes

$$\frac{\partial M_r}{\partial r} \;=\; \frac{\partial M_r}{\partial [r_0(1 + r^1/r_0)]}$$

The perturbed form of this equation is

$$\frac{\rho^1}{\rho_o} \;=\; -\,3\frac{r^1}{r_0} \;-\; r_o\,\frac{\partial (r^1/r_0)}{\partial r_0} \quad (eq.\ Ip - radial)$$

The force equation for the radial case is HKT eq. 8.2,

$$\frac{d^2 r}{dt^2} \;=\; -\;4\pi r^2\,\frac{\partial P}{\partial M_r} \;-\; \frac{GM_r}{r^2} \quad (eq.\ III\ radial),$$

with the perturbed version being HKT eq. 8.7.

Through substitution and differentiation, in a manner similar to what we did earlier to derive the speed of sound, we construct the linearized adiabatic wave equation (LAWE). Details are given § 8.1 of HKT. We then look for sinusoidal solutions, separating the radial and time dependence,

$$\frac{r^1(t, r_0)}{r_0} \;=\; \frac{r^1(r_0)}{r_0}\, e^{i\sigma t}$$

where σ may turn out to be complex; if it is real, $\sigma = \omega$.

The LAWE is difficult to solve. We consider for illustrative purposes a simpler case, setting the wave amplitude independent of r. We then find, for the constant density model,

$$(3\gamma - 4)\, \frac{4\pi G}{3}\, <\rho> \;=\; \sigma^2.$$

If $\gamma > 4/3$, σ is real, and the corresponding period Π is

$$\Pi \;=\; 2\pi/\sigma \;=\; \frac{2\pi}{\sqrt{(3\gamma - 4)\; <\rho>\; 4\pi G/3}}$$

If $\gamma < 4/3$, the perturbation either grows or decays exponentially. This does not correspond to radial pulsations; the "period" is the approximately the free fall time (the dynamical timescale).

For the radial modes, the stellar surface swells and contracts, the surface temperature and emitted flux change over the period, and the amplitude of variation observed is much larger than for the small amplitude non-radial modes seen in the Sun. The overtones do not have a node at the surface either. (Fig.-8.1 of HKT shows the radial displacements as a function of r/R calculated for the fundamental and first two overtone modes in a $n = 2$ polytrope).

The stars we normally consider variable stars (Cepheids, RR Lyraes, etc) are radially pulsating stars.

Our dispersion relation for pressure waves is $(\omega^2 - \omega_c^2) = c_s^2 k_z^2$ for the constant temperature case. For $\omega^2 >> \omega_c^2$, we have $\omega^2 = c_s^2 k_z^2$. The fundamental mode has $\lambda = 4R$ and $k_z = 2\pi/(4R)$.

Since $c_s^2 = \gamma P_0/\rho_0$, the period Π of the mode is then

$$\Pi \;=\; \frac{2\pi}{\omega} \;=\; 4R\sqrt{\frac{\rho_0}{\gamma P_0}}.$$

We use the equation of hydrostatic equilibrium in its approximate form

$$\frac{dP}{dr} \;=\; -\rho g \;=\; -\rho\, G\, \frac{M}{R^2} \;\approx\; \frac{< P >}{R}.$$

So $< \rho > / < P >= R/GM$, and $\Pi \propto 1/\sqrt{\gamma\ \rho\ G}$.

Doing this more carefully, one obtains

$$\Pi \;=\; \sqrt{\frac{3\pi}{(3\gamma - 4)\ G\ \ < \rho >}}$$

Substituting values for the Sun, we find for the fundamental radial mode of pulsation:

$$\Pi \;=\; 0.04\ \sqrt{\frac{< \rho_\odot >}{< \rho >}}\ \text{days}$$

Since the mean density of stars varies enormously from $10^6 > \frac{<\rho>}{<\rho_\odot>} > 10^{-9}$ there is an enormous range in the period of the fundamental mode of pulsation, from 3 sec to 1000 days. Harmonics have smaller λ, larger k_z, and shorter periods. In all cases, the surface $r = R$ is not a node of the motion.

For the isothermal atmosphere discussed above, we find that the oscillation eigenvalue is proportional to $e^{z/H}\ e^{i(\omega t - k_x x - k_z z)}$. (By symmetry we do not need to consider the third axis, i.e. we use k_x here instead of $\sqrt{k_x^2 + k_y^2}$, ignoring rotation, magnetic fields, etc. which would distinguish the k_x and k_y terms.) Since the pressure scale height $H = P_0/(\rho_0 g)$, the amplitude of the oscillation decreases as the temperature increases. Thus the largest amplitude is near the surface. The amplitude in the core is decreased by the very large ratio of $\rho(core)/\rho(surface)$. We can thus ignore any pulsations in the core, and this implies that variations in the nuclear energy generation rate ϵ cannot drive pulsations.

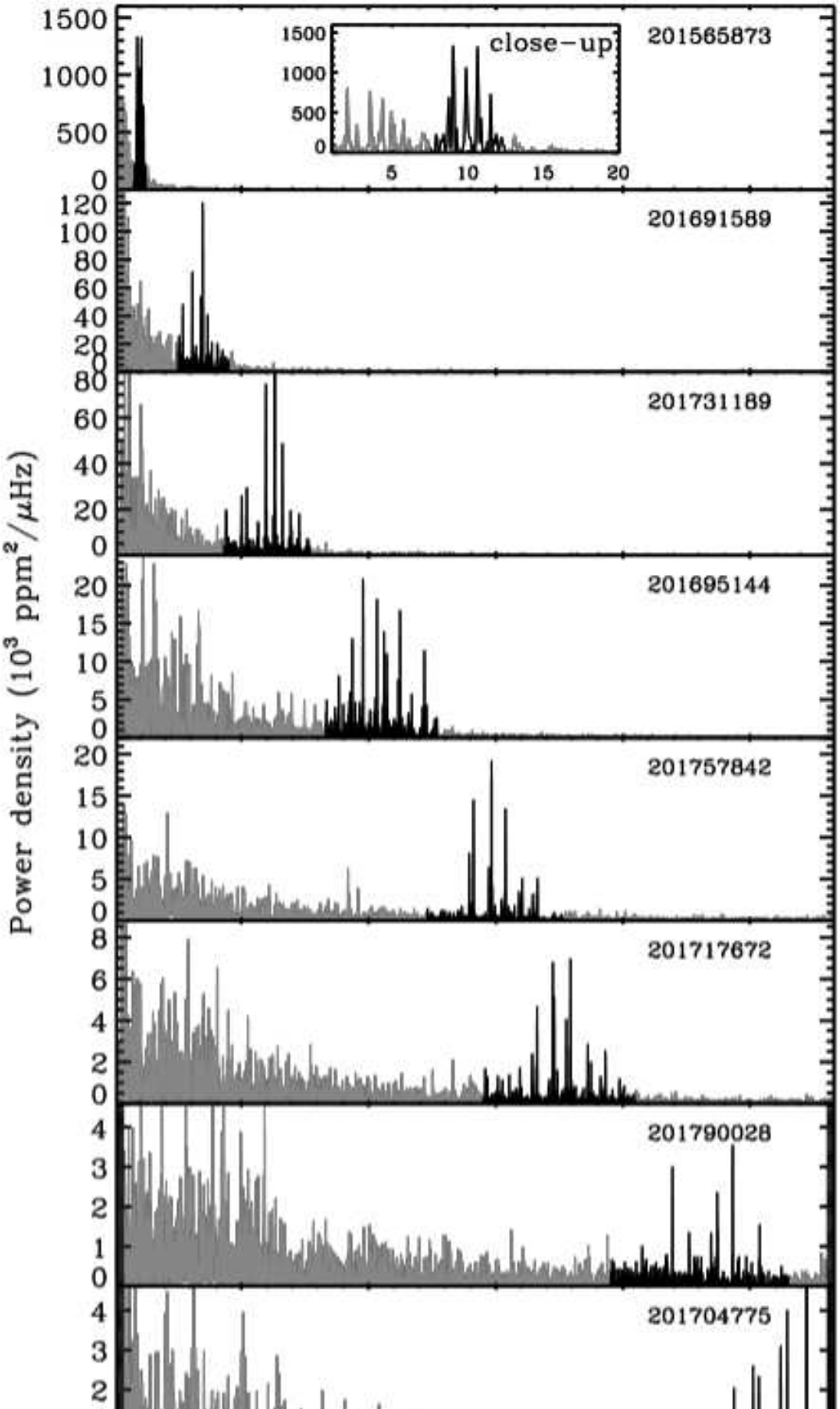
close−up
201565873
201691589
201731189
201695144
201757842
201717672
201790028
201704775
Power density (10^3 ppm^2/μHz)

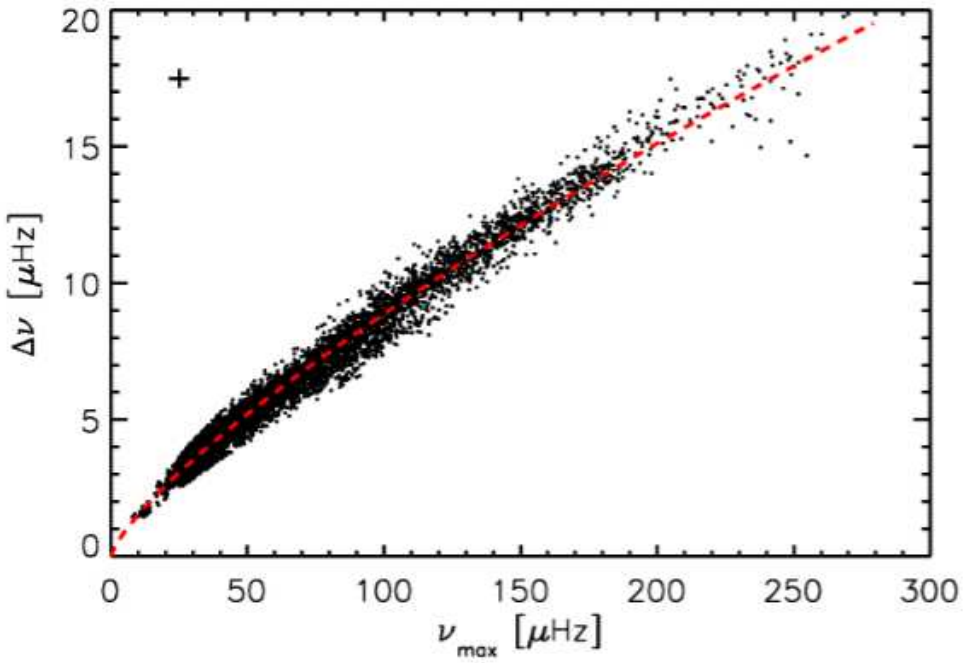

Figure 3. $\langle \Delta\nu \rangle$ versus $\nu_{\rm max}$ for the oscillating red giants with the characteristic uncertainty shown with a cross in the left top corner. The red dashed line indicates the power-law fit through the results (see text).

Fig. 14.— Fig. 3 of Hekker, Gilliland, Elsworth et al, 2011, arXiv:1101.0141. The evolution of red giants in their mode characteristics as they climb the giant branch.

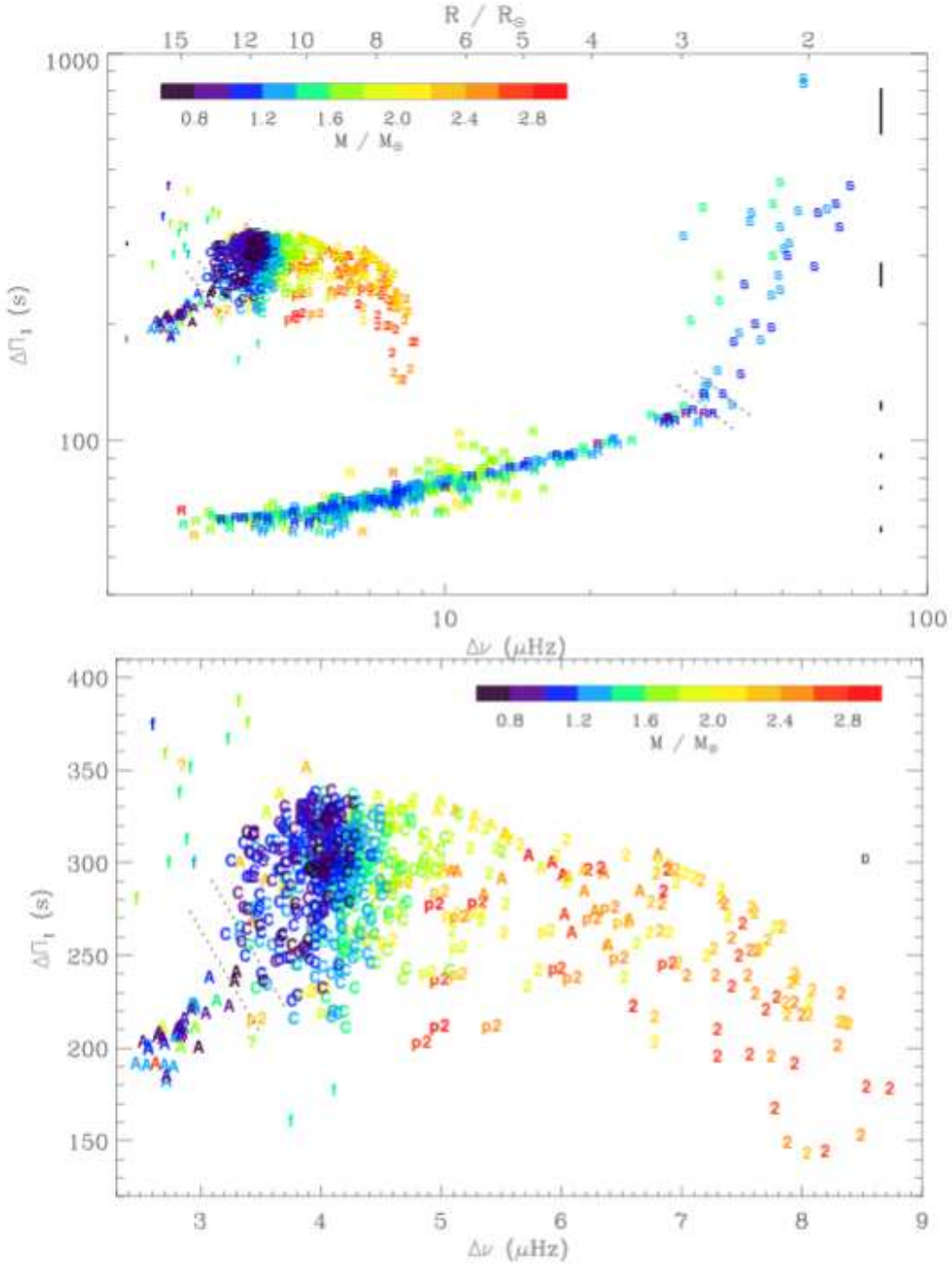

Fig. 1. Period spacing $\Delta\Pi_1$ as a function of the frequency spacing $\Delta\nu$. **Top:** The seismic proxy for the stellar mass is indicated by the color code. The evolutionary states are indicated by S (subgiants), R (RGB), f (helium subflash stage), C (red clump), p2 (pre secondary clump), 2 (secondary clump), and A (stars leaving the red clump moving toward the AGB). The error boxes on the right side indicate the mean uncertainties, as a function of $\Delta\Pi_1$, for stars on the RGB; for clump stars, uncertainties are indicated on the left side. Dotted lines indicate the boundaries between evolutionary stages. **Bottom:** Zoom in the red-clump region. Data used in this figure are available at the CDS.

Fig. 15.— Fig. 1 of Mosser, Benomar, Belkacem, et al (2015) (arXiv:1411.1082) showing the mode behavior for stars climbing the RGB from subgaitns to the RGB tip, then clump stars. The colors denote the stellar mass.

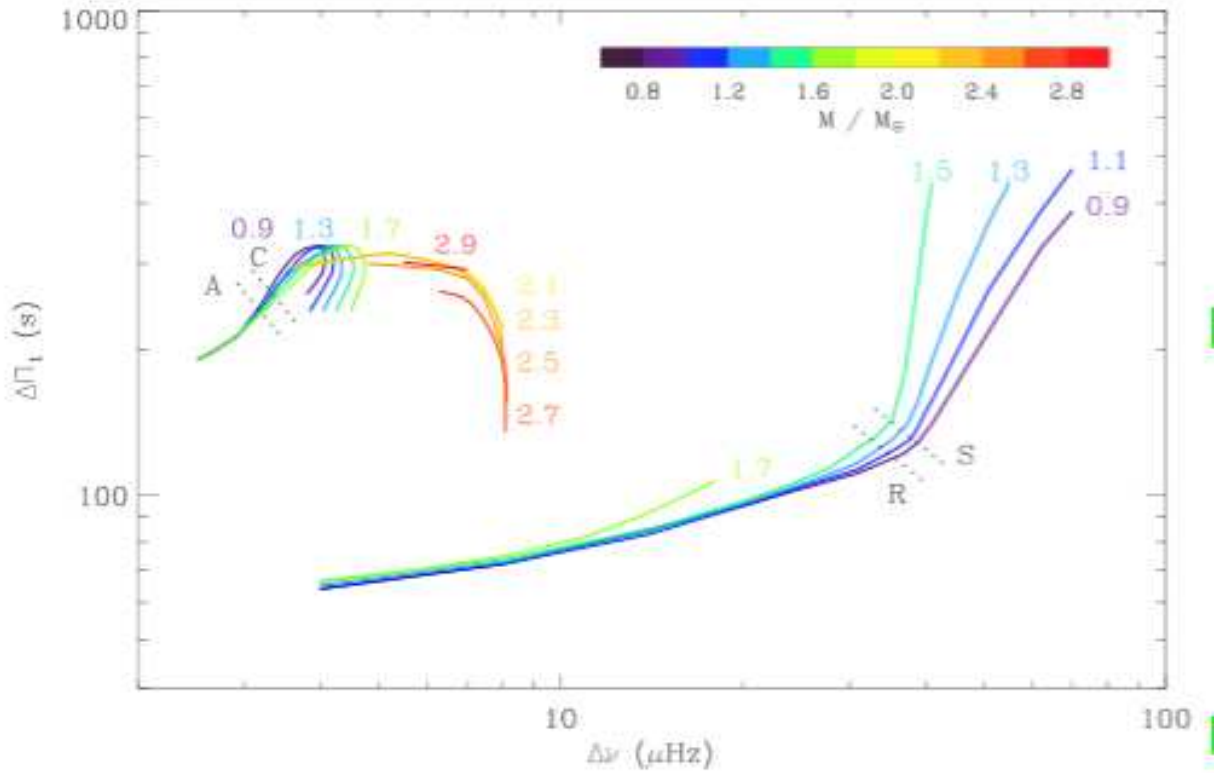

Fig. 2. Evolutionary tracks reconstructed from the seismic observations for stellar masses in the $[0.9 - 2.9\,M_\odot]$ range. The $1.9\,M_\odot$ track is not shown because more information is needed to define the limit between the clump and secondary-clump stars. On the RGB, the dispersion due to the first luminosity bump is too high to allow an unambiguous definition of the evolutionary tracks for stellar masses above $1.9\,M_\odot$. Dotted lines indicates the boundaries between evolutionary stages.

Fig. 16.— Fig. 2 of Mosser, Benomar, Belkacem, et al (2015) (arXiv:1411.1082). The colors denote the stellar mass.

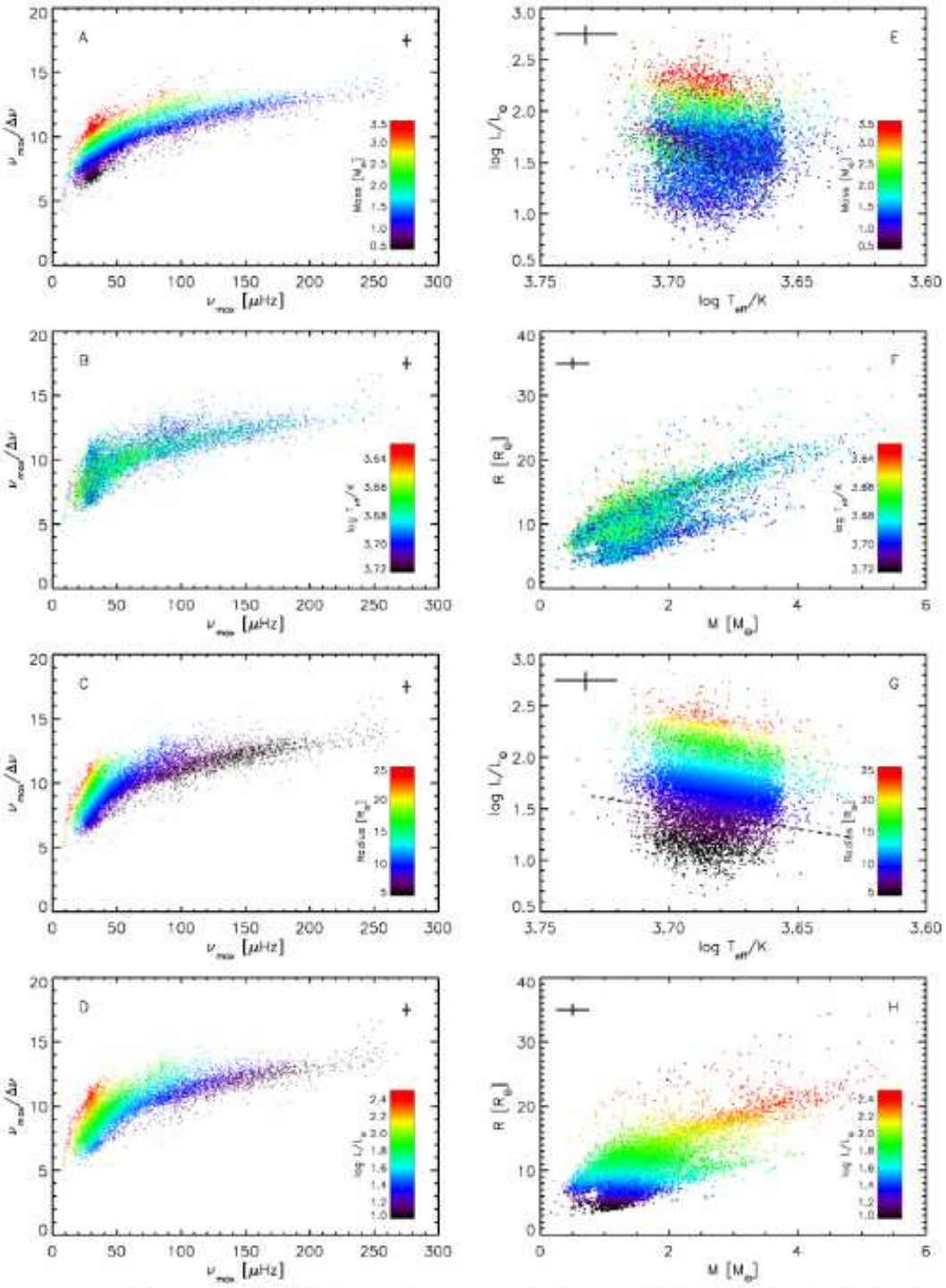

Figure 5. ν_{max} versus $\nu_{max}/\langle\Delta\nu\rangle$ diagrams (left) and H-R diagrams and mass versus radius diagrams (right) of the public red giants with detected oscillations. The colour-coding indicates from top to bottom mass, effective temperature, radius and luminosity. The highest and lowest values in the colour scale are lower and upper limits, respectively, to enhance the colour contrast. Characteristic uncertainties are indicated with a cross in the corner of each panel. The black dashed line in panel G indicates a radius of 7.5 $R_\odot$ (see text).

Fig. 17.— Fig. 5 of Hekker, Gilliland, Ellsworth et al, arXiv:1103.0141. Mode diagrams for RGB stars illustrating the dependence on various stellar parameters. The colors denote the stellar mass.

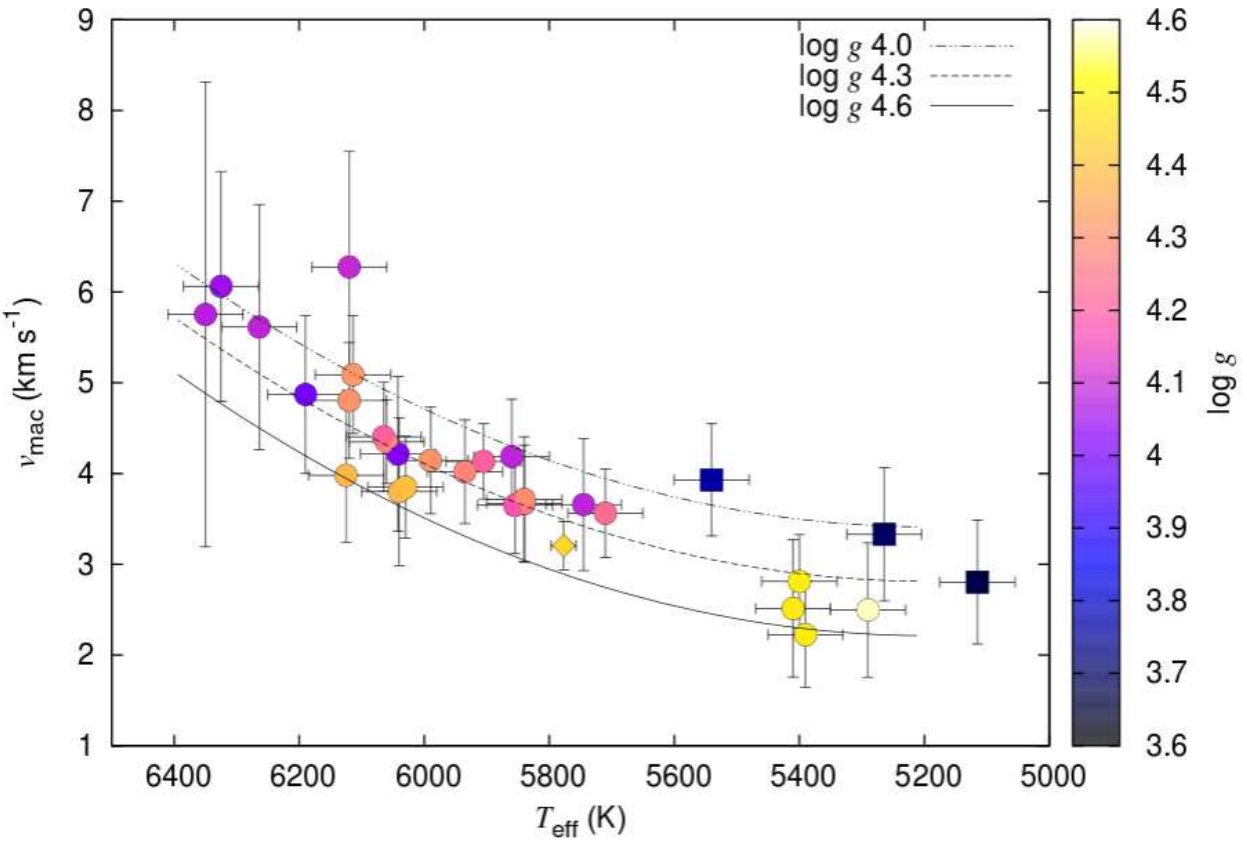

Figure 2. Macroturbulence is seen to increase with increasing $T_{\rm eff}$, however there also seems to be some $\log g$ dependence. The circles represent the stars used in this study, the diamond represents the Sun, and the squares are the red giants from Deheuvels et al. (2014). The red giants are not included in the calibration.

Fig. 18.— Fig. 4 of Doyle, Davies, Smalley et al (arXiv:1408.3988) illustrating the determination of stellar macroturbulence via asteroseismology. This quantity can also be determined from analyzing the widths of spectral lines. The vertical axis on the left is v_{max} in km/sec, and on the right is color key for the surface gravity. The colors denote the stellar mass. The curves represent model predictions for $\log(g)$ 4.0, 4.3, and 4.6.

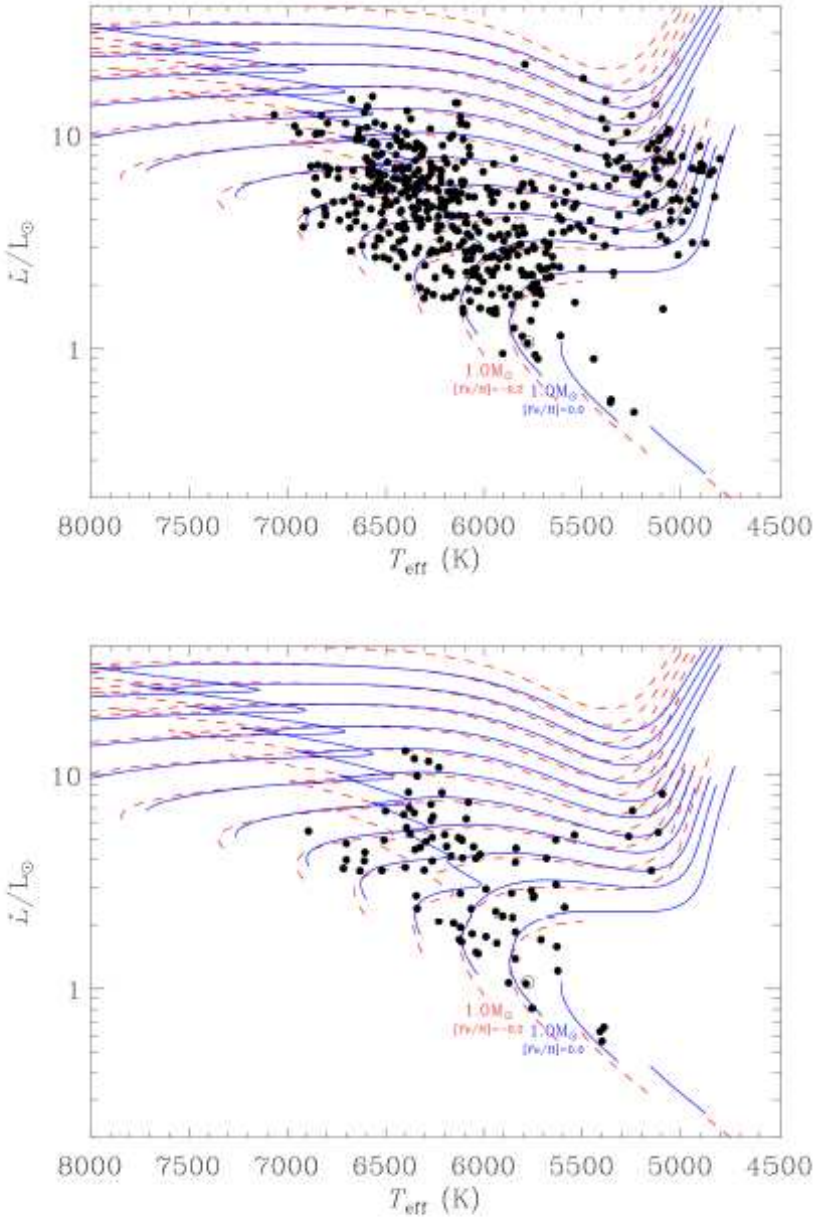

Fig. 3.— Top panel: HR diagram of the full cohort of stars. Temperatures are from the IRFM set; luminosities were calculated using the asteroseismically estimated stellar radii presented later in the paper, in Table 5. Bottom panel: HR diagram of the smaller cohort with spectroscopic $T_{\rm eff}$ and [Fe/H]; luminosities were estimated using the radii presented in Table 6. The evolutionary tracks in both panels were computed at $0.1\,M_{\odot}$ intervals with the YREC code. Tracks in blue (solid lines) are for solar composition, those in red (dashed lines) for [Fe/H]$= -0.2$. The models are not "solar calibrated" models and hence the $1\,M_{\odot}$ tracks need not pass through the exact location of the Sun.

Fig. 19.— Fig. 3 of Chaplin, Basu, Huber et al (arXiv:1310.4001). The blue isochrones are for solar composition, the red ones are for a star with a star with $\sim 60\%$ of the solar

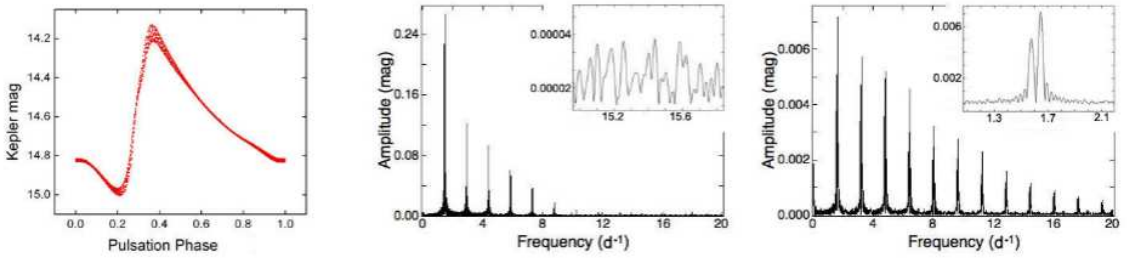

FIG. 1.— **Left:** Light curve of KIC 5559631 folded with the main period of 0.620699 d. The spread in the width of the light curve is not noise (which is much smaller than the size of the data points), but shows the amplitude and phase modulation over the 27.6-d Blazhko cycle. **Middle:** Fourier Transform of the raw data converted to the magnitude scale. The insert shows the noise level. **Right:** Fourier Transform after prewhitening with the main frequency and its harmonics. The insert is a zoom, on the same scale, around the position of the main frequency and its harmonics. Triplet components are clearly detected.

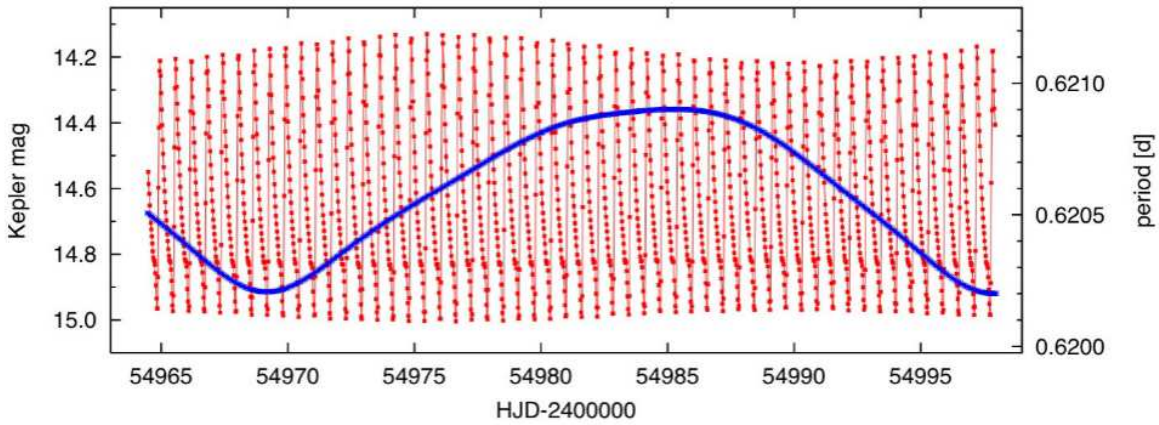

FIG. 2.— Relationship between the period change and amplitude modulation over the Blazhko cycle for KIC 5559631. The red dots show the Kepler data, the red line our multi-frequency fit to the data. The blue line shows an instantaneous period determined using the analytical signal method (units to the right side of the panel). The period change cannot be a Doppler shift caused by a companion, as that would imply an orbital velocity of the RR Lyrae star about the barycentre of about 200 km s^{-1}, requiring an impossibly large mass for the companion.

Fig. 20.— Figs. 1 and 2 of Kolenberg, Szabo, Kurtz et al, arXiv:1001.0417, "First Kepler results on RR Lyrae stars". The Blazko effect (whose origin is unknown) is subtle, here, but much stronger in the next figure.

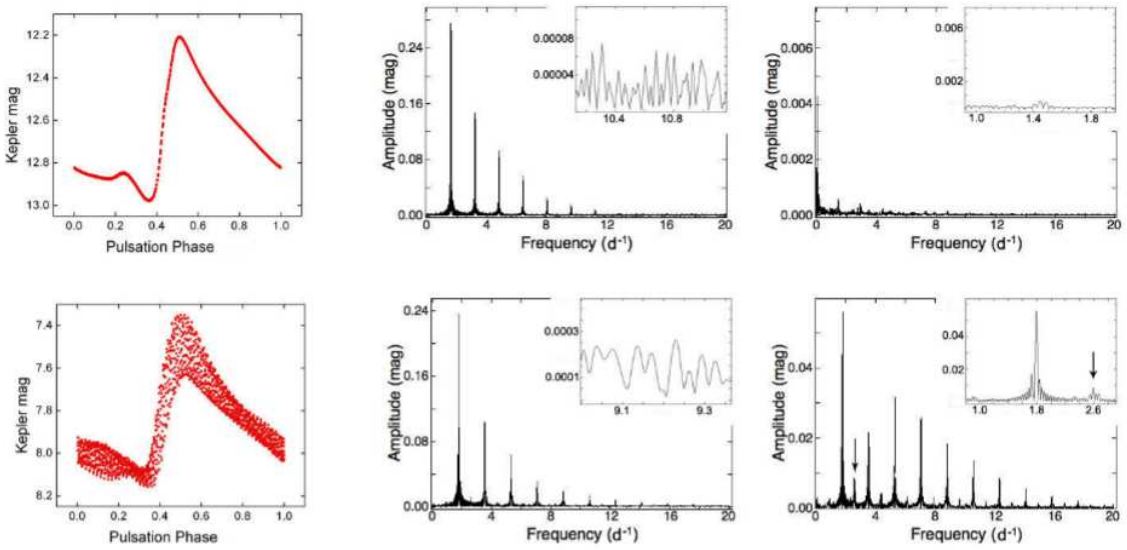

FIG. 3.— **Left:** Light curves of two *Kepler* RR Lyrae stars (KIC 3733346 and KIC 7198959) folded with the main period. **Middle:** Fourier Transform of the raw data converted to the magnitude scale. The insert shows the noise level. **Right:** Fourier Transform after prewhitening with the main frequency and its harmonics. The insert, on the same scale, is a zoom around the position of the main frequency and its harmonics. For the modulated star (KIC 7198959) multiplet components are clearly detected. Arrows point at the highest peak connected to an additional frequency.

Fig. 21.— Fig. 3 of Kolenberg, Szabo, Kurtz et al, arXiv:1001.0417, "First Kepler results on RR Lyrae stars". Note the strong Blazko effect (whose origin is unknown) in the RR Lyr star whose light curve properties are displayed in the lower set of panels.

6. Wave Excitation

Stellar pulsation is a long term phenomena; the pulsations are stable and persist over many cycles. Pulsations begin if/when the star is unstable for small displacements of a parcel of gas. There is always some small random $\delta P = P - P_0$ present. Pulsations grow in amplitude until non-linear effects limit the growth to the observed finite amplitudes. Pulsations die out when a star evolves into a configuration that is stable against pulsations. On such a very long timescale, pulsations are transient phenomena.

Energy must be fed into the pulsations via some driving mechanism to sustain them. Over most of the interior of the star, energy is lost during each pulsation cycle, and this effectively damps the pulsation. But in some radial region(s), there must be energy fed into the pulsation, enough to overcome the effect of all the damping from other regions, for the pulsation to persist.

Consider the angular frequency $\omega = \omega_1 + i\omega_2$ where ω_1 and ω_2 are both real. To get sustained propagating waves, ω_2 must be zero. If it is not, then the waves, once excited, will either exponentially increase or decrease in amplitude so that the pulsation dies out, not pulsate at a fixed amplitude over a long period of time.

A second requirement is that the pulsation becomes established on a timescale which is less than the evolutionary timescale of the star, $\sim 10^9$ yr for main sequence stars, smaller for more evolved stars.

To evaluate ω requires using a non-adiabatic energy equation instead of assuming adiabatic motions of the gas. This is very difficult, see Cox & Guili §27 for a discussion. One finds that the existence of instability is related to the position of envelope ionization zones, often of He II, as that often falls in about the right temperature and radius of the star.

To evaluate this, we must consider the work done by the gas element as it expands and then contracts. dQ, the work done on the element (i.e. the heat added to the parcel of gas) is $dU + dW$, where dW is the work done by the parcel of gas on its surroundings. Over the cycle, the integral of dU must be 0 since the beginning and end state are identical. A region which gains heat during the compression part of the cycle drives the pulsation, while regions that lose heat during the compression damp the pulsation.

W is the work done by the gas during the cycle, $W = \oint dQ$. Work is available to drive the oscillation if $\oint dQ > 0$. Since the entropy S is constant, $\oint dS = 0 = \oint dQ/T$. (Note that if T is constant throughout the cycle, $\oint dQ = 0 = W$ and there cannot be pulsations.)

Assume $T(t)$ has a cyclic modulation, $T(t) = T_0 + \Delta T(t)$.

$$0 \;=\; \oint \frac{dQ(t)}{T_0 + \Delta T(t)} \;\approx\; \oint \frac{dQ(t)}{T_0}(1 - \Delta T/T_0)$$

Then

$$W \;=\; \oint dQ(t) \;=\; \oint dQ(t)\frac{\Delta T(t)}{T_0}$$

To have $W > 0$ integrated over a cycle requires that ΔT is positive when $dQ(t)$ is positive (heat is added to the element when the temperature is higher) and ΔT is negative when $dQ(t)$ is negative (heat is lost from the parcel of gas when T is low).

A star can pulsate if

$$W(total) \;=\; \int_0^M [\oint \frac{\Delta T}{T_0(m)}\, dQ(m)]\, dm \;>\; 0.$$

A careful study of this integral (the original early work is by Epstein, 1950, ApJ, 112, 6) suggests that the region of highest weight in the integral is at $r \sim 0.7R$.

Nuclear reaction rates behave to drive pulsations, ϵ increases rapidly when T increases, and the sign is correct for $W > 0$. However, as indicated above, the pulsational amplitudes are very low in the stellar core and the integral over the nuclear burning regions is not big enough to overcome what may be happening in the outer parts of the star. This potential mechanism does not seem to be causing pulsations in any known category of stars.

For most large amplitude pulsating stars, including all radial pulsators, the driving mechanism is related to the opacity, hence called the κ-mechanism. For this to work, the opacity must be large, thus usually from H or He. If one has an opacity κ such that κ increases when the star contracts, energy can be removed from the radiative flux at the proper time to drive oscillations. The mechanism involves a region with high H, HeI or HeII opacity which blocks the radiation from flowing outward, then the pressure increases, the star swells outward past the equilibrium point. Ionization then reduces the opacity, radiation flows through, the gas cools, the pressure drops so that the layer can no longer support the upper layers, and the star shrinks back. The stellar $T(r)$ and $P(r)$ define radial regions where strong ionization is ocurring for H and/or He, and these must lie in the key region $r/R_* \sim 0.7$ in order to achieve long term stable pulsationals. This occurs only within small regions of the HR diagram; this constraint is the origin of the "instability strip" of various types of variable pulsating stars in the HR diagram (see Fig. 9 and Fig. 10.

The mode in which a star pulsates is determined by the local thermal time scale of the driving zone, given by

$$\tau_{th} \;=\; \int_r^R \frac{c_p T}{L}\, dm,$$

where L is the star's luminosity. This is often much smaller than the global thermal timescale for the entire star.

The oscillation period needs to be comparable to or smaller than τ_{th} in the driving zone. If it is larger, $\Pi >> \tau_{th}$, the driving layer remains in thermal equilibrium and pulsation in the mode with period Π is not excited. Determination of which modes are excited is very complex and requires extensive calculations for a specific detailed model stellar atmosphere.

One can show that a radial zone with no nuclear energy generation is stable if

$$f(m) = \frac{4}{c} - (\frac{\kappa_T}{c} + \kappa_P) - \frac{4}{3\gamma} > 0, \quad \kappa_T = \frac{\partial ln\kappa}{\partial lnT}|_P \quad \text{and } \kappa_P = \frac{\partial ln\kappa}{\partial lnP}|_T,$$

and γ is the adiabatic index from $P \propto \rho^\gamma$. c here is from another adiabatic index, $PT^{\gamma_2/(1-\gamma_2)} =$ constant, and $\gamma_2 = c/(c-1)$. γ and c (from γ_2) are evaluated for adiabatic changes.

$4/c$ is always positive, so always promotes stability, but the opacity derivitives can be destabilizing if κ_T and/or κ_P are positive. The last term is always destabilizing (it arises from the spherical geometry). If the integral of $f(m)$ over the mass of the star is positive, the star is stable against pulsation.

We recall that in ionization zones, all of the adiabatic indices γ approach 1, c (from γ_2) becomes very large, $4/c$ in the above expression for $f(m)$ approaches 0, as does κ_T/c, and κ_P is always positive. The contribution of low γ is called the γ-mechanism, which often acts together with the κ-mechanism. Ionizing regions do not heat up when compressed. Also in ionization zones, ionizing the gas reduces the opacity and causes a contraction of the star. After the contraction, the ion recombines, the opacity rises, flux is absorbed, etc. Thus an ionizing zone with radiative transfer can become unstable to pulsations.

It is very complicated to evaluate the total effect of this over the entire star, as some regions drive and others damp the pulsations.

While normally the ionization zone of H or He II is the crucial one, in certain cases the κ-mechanism can be driven by ionization of Fe group elements. This can occur if suitable diffusion (gravitational settling) enhances the abundance of these elements by large factors (at least several powers of 10) within the star at crucial radii.

The low amplitude non-radial oscillations seen in the Sun, and also in most similar stars that have been studied in sufficient detail, are presumably excited by stochastic variations arising within a convection zone. We expect, and observations seem to bear this out, that any star with a convection zone near its surface, will show low amplitude non-radial oscillations.

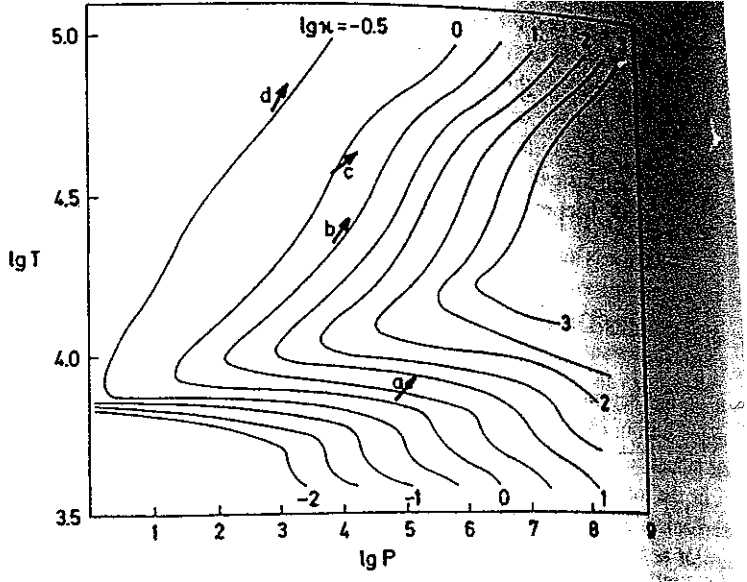

Fig. 41.1 Lines of constant opacity κ in the $\lg P$–$\lg T$ plane (all values in cgs). Four *arrows* are shown that indicate the direction in which a mass element moves during adiabatic compression. For the *arrows* labelled *a*, *b*, and *d*, the direction is given by $\nabla_{ad} = 0.4$. In case *a* the *arrow* points in the direction of increasing κ, i.e. the κ mechanism has a "driving" effect on pulsations. In cases *b* and *d* the *arrows* point in the direction of decreasing κ, indicating a "damping" (or almost neutral) effect on pulsation. In case *c* the direction of the *arrow* is different from that of the other ones, since ∇_{ad} is here reduced by the second ionization of helium. Because of this reduction, the *arrow* points in the direction of increasing κ, and this ionization region can contribute considerably to the excitation of pulsations in Cepheids

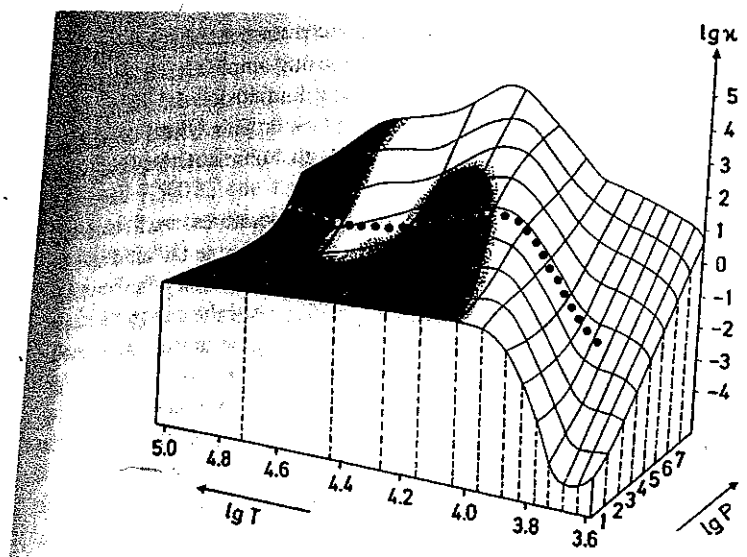

Fig. 41.2 An opacity surface ("κ mountain") for the outer layers of a star as in Fig. 17.6. But this time the dependence with respect to P (in dyn cm^{-2}) and T (in K) is shown. The *dotted line* corresponds to the stratification inside a Cepheid of $7M_\odot$. The *white areas* of the "mountain" indicate regions which excite the pulsation and the *black* ones those which damp it. The excitation in the region of $\lg T \approx 4.6$ is due to the second ionization of helium

Illustration of the κ (opacity) method of inducing oscillations from Kippenhahn, Weigert & Weiss, Stellar Structure & Evolution, 2nd edition (textbook)

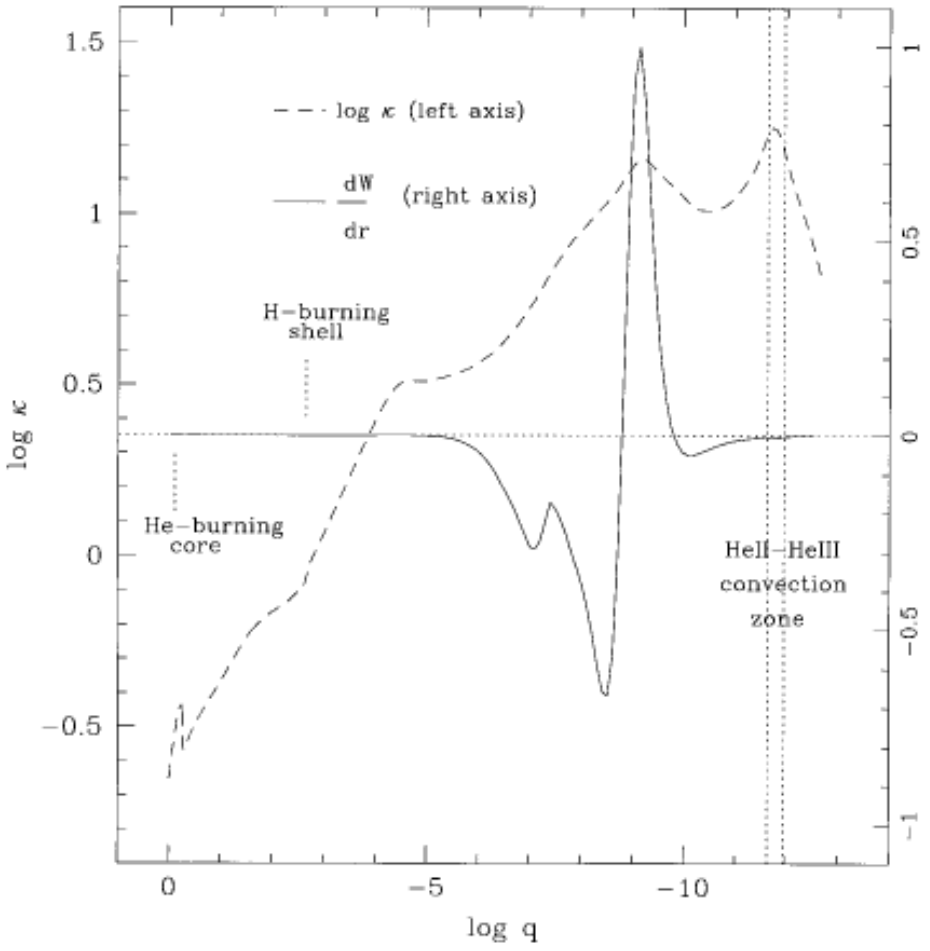

FIG. 1.—Run of the integrand of the work integral for the f-mode with $l = 2$ (*solid curve*) and of the Rosseland opacity (*dashed curve*) vs. fractional mass depth in a typical subdwarf B model. The locations of the He-burning core, the residual H-burning shell, and the He II–He III convection zone are indicated. The driving region (positive values of dW/dr) is clearly associated with an opacity bump, itself caused by heavy-element ionization.

Fig. 22.— Predicted Fe abundance and Rosseland mean opacity as a function of fractional mass depth q ($q = log[1 - M(r)/M_*]$ for a model of a subdwarf B star. Unlike the paper from which the next figure was taken, this paper was written after the predicted oscillations in this type of star had been observed. Opacity bumps are from ionization of FeII (deeper one) and from ionization of H (closer to stellar surface). (From Charpinet et al, 1997, ApJL, 483, L126)

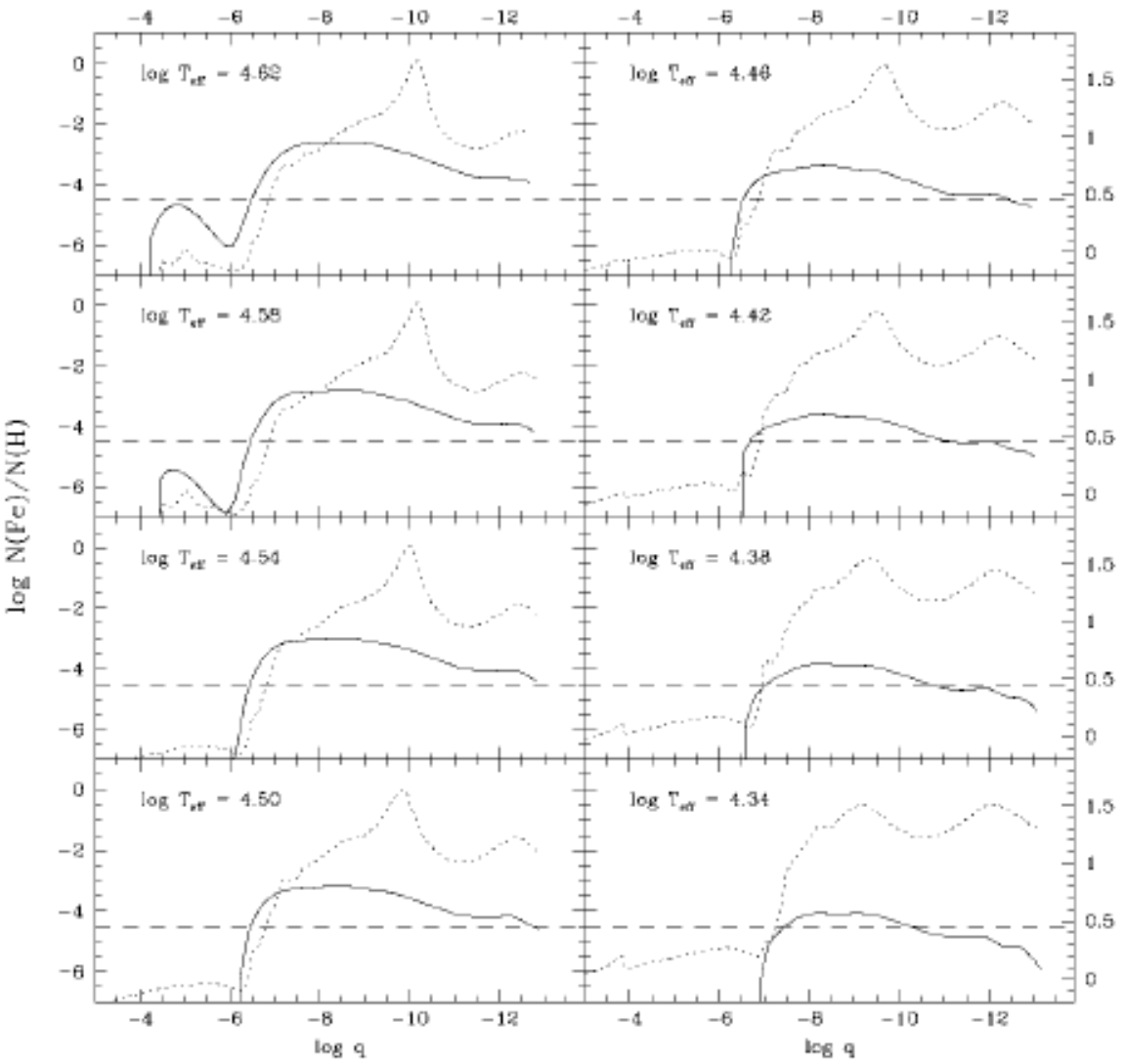

FIG. 1.—Equilibrium abundance of iron (*solid curve*) as a function of the fractional mass depth $\log q$ [$= \log (1 - M(r)/M_*)$] for a series of representative models of sdB stars with $M = 0.48\ M_\odot$, $\log g = 5.8$, and $\log T_{\rm eff}$ from 4.34 to 4.62 in steps of 0.04. In each panel the tip of the solid curve on the right hand side corresponds to the location of the Rosseland photosphere. The dashed horizontal line gives the normal value of the *Fe/H* number ratio. Also shown is the profile of the Rosseland opacity (*dotted curve*); its logarithmic value can be read on the right axis.

Fig. 23.— Predicted driving and damping regions for subdwarf B stars from Charpinet et al, (1996, ApJL, 471, L103) They predicted oscillations would be found in such stars BEFORE any asteroseismology observations of them had been made.

7. Taxonomy of Pulsating Stars

Normal radial pulsators, which have the largest amplitude of integrated light and radial velocity variations, obey $\Pi \sqrt{<\rho>} =$ constant, where Π is the period of the pulsator. Since $<\rho> = (4\pi/3)M/R^3$ and $L = 4\pi R^2 \sigma T_{eff}^4$, we get

$$<\rho> \ \propto \ M \ [\frac{T_{eff}^4}{L}]^{3/2}, \qquad \frac{\Pi \sqrt{M} \ T_{eff}^3}{L^{3/4}} \ = \ \text{constant}.$$

Thus for homologous stars, where M and T_{eff} and L are all related to each other by power laws, we end up with a period – luminosity law which is valid for a particular type of variable star within a small range of M and T_{eff}.

The $P-L$ law (usually expressed as $M_X \ = \ A \ log(P)+B$; here M_X is a magnitude (i.e. brightness) at wavelength band X). Determining the constants A and B for the Cepheid $P-L$ law requires observation of Cepheids at known distances at the specific wavelength bandpass (denoted X) desired. Even if one uses "nearby" Galactic Cepheids, this is difficult as Cepheids are luminous stars. Even bright Cepheids are distant, too distant for accurate parallax measurements using standard techniques. Furthermore since they are located in the Galactic plane, their reddenings are high. The recent determination of parallaxes for 9 nearby Milky Way Cepheids using the HST fine guidance sensors by Benedict, McArthur, Feast et al (2007, AJ, 133, 1810) has provided accurate distance determinations to a small number of nearby Cepheids, which can be used to calibrate the $P-L$ relationships at a specific wavelength.

These period–luminosity laws have been very important in establishing distances to various types of variable stars, predominantly Cepheids and RR Lyr stars, which can be found and monitored in nearby galaxies with ground based telescopes in sites with good seeing (for the nearest galaxies) or with HST for somewhat more distant ones. This in

turn is a key step in the distance ladder for more distant galaxies, determining the Hubble constant, etc. There are several factors such as metallicity which have small effects on the period – luminosity relation which must be taken into account for accurate distance determinations.

Radial pulsators include the δ Scuti stars, the Cepheids and RR Lyrae stars (both of which can be double mode pulsators in narrow ranges of ΔL and ΔT_{eff}). These stars are crossing the instability strip (the region where radial pulsation can occur is a strip in the HR diagram slanting from high L, lower T_{eff} to lower L and higher T_{eff}, see the appended figure) for the second time. Third crossing Cepheids are called BL Her stars, higher crossings are called W Vir stars. Then there are the semi-regular and Mira variables, cool and with high luminosities.

The position of the instability strip in the H-R ($L - T_{eff}$) diagram can be derived, but is complicated. It is based on requiring the ionization zone to be at the right depth in the star; see the earlier discussion of driving mechanisms for pulsation. The arguement involves the depth within the star of He II ionization region, located in mass ΔM below the surface of the star. The temperature at that depth is fixed by the requirements for ionization of He II to be ocurring. The pressure at that depth is fixed by having to support the overlying mass ΔM. The region must also be located where the thermal timescale becomes approximately equal to the dynamical timescale, so that in the deeper layers pulsations are adiabatic, but at the transition layer and higher, the pulsations are not adiabatic as the thermal timescale is small due to the low density. From this, the location of the instability strip as a function of stellar luminosity and T_{eff} can be derived. One gets for the predicted instability strip

$$L \propto T_{eff}^{-20},$$

close to the very steep observed instability strip of fundamental mode pulsators. Adding in an expression for the luminosity of a He-core burning star in the region of the instability strip from stellar models (HKT adopts $L \propto M^{9/2}$), one can predict (roughly) the period – radius and period – luminosity laws, $\Pi \propto R^{1.31}$ and $\Pi \propto L^{0.79}$, both of which are close to the observed properties of fundamental mode pulsators such as Cepheid variables.

The ratios of periods for stars pulsating in two radial modes, i.e. the fundamental and first overtone radial modes, is a key test of pulsation theory and of stellar models. Another key test is to compare evolutionary masses for stars of known distance with the pulsational masses; this is usually applied to Cepheid variables.

Mira variables (luminous AGB stars) become pulsationally unstable as they evolve up the AGB. They begin pulsating in the first overtone, but as they evolve up the AGB to still higher L, they switch to the fundamental mode. At that time the pulsation amplitude becomes very large, substantial mass loss then follows, and the stars become obscured at optical wavelengths by the ejected material, but very bright in the infrared. (see papers on OH/IR stars by Wood and others)

Observations of light curves for many bright high amplitude variable stars have been obtained for many years as they are good targets for amateur astronomers. The brighter variable stars have light curves compiled by the AAVSO (American Association of Variable Star Observers, a group of amateur astronomers) extending over 25 years or more. Cepheids, for example, may vary in light at V by about 1 mag, and have radial velocity variations across the cycle of ~ 50 km/sec. Period changes can be measured for some Cepheids and other pulsating stars, see the review by H. Smith (2013, arXiv:1310.0533), for example. Typical measured period changes for Cepheids are ~ 0.1 second/year, hence detectable over about a decade. A comparison of measured period changes versus those predicted from a combination of the theory of stellar evolution and pulsational theory provides a crucial test

of the validity of the stellar evolutionary theory.

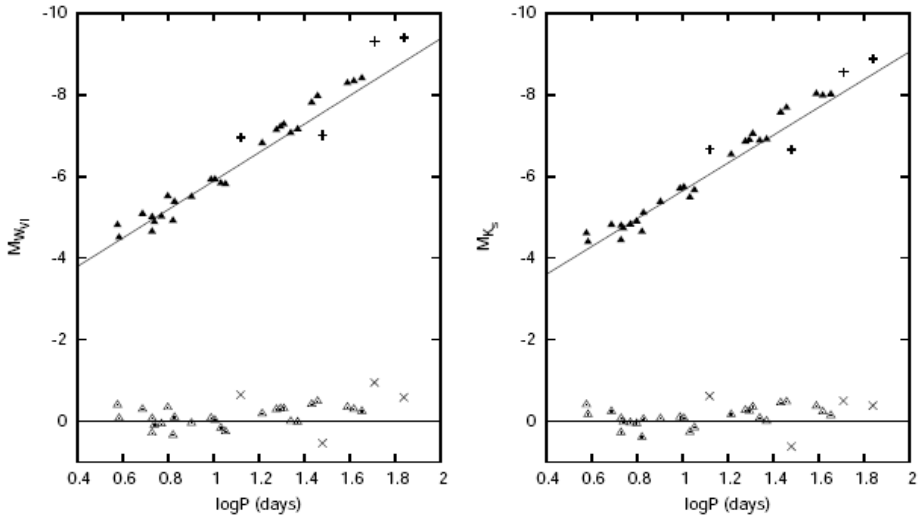

Fig. 1. Comparison of absolute magnitudes derived from ZAMS parallaxes (triangles) for 30 stars with the *PL* relations based on 54 IRSB parallaxes in W_{VI} and K_S bands (solid lines). The bottom panel shows residuals with respect to the IRSB *PL* relations. Long-period Cepheids appear to be progressively shifted. Rejected stars (see text) are marked with pluses and crosses.

Fig. 24.— Period luminosity law for Galactic Cepheids with the most accurate distances for the V and the K bandpass. The plot is log(period) vs. log(1/Luminosity) because the magnitude scale is logarithmic and inverted (smaller mag $\equiv$ fainter L). Fig. 1 of Fouque, Arriagada, Storm et al, 2007, A&A (in press) (see Astro-ph/0709.3255)

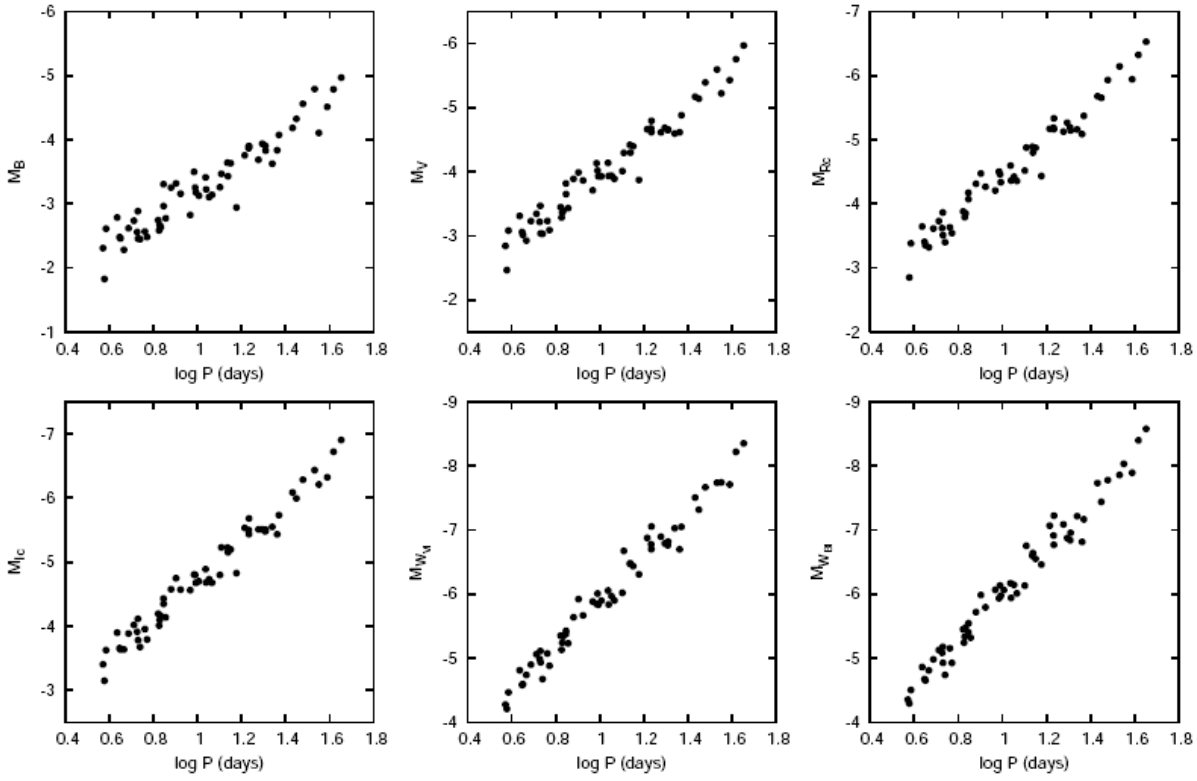

Fig. 2. Adopted Galactic *PL* relations in optical bands.

Fig. 25.— Period – luminosity relations for Galactic Cepheids using various optical bandpasses. Fig. 2 of Fouque, Arriagada, Storm et al, 2007, A&A (in press) (see Astro-ph/0709.3255)

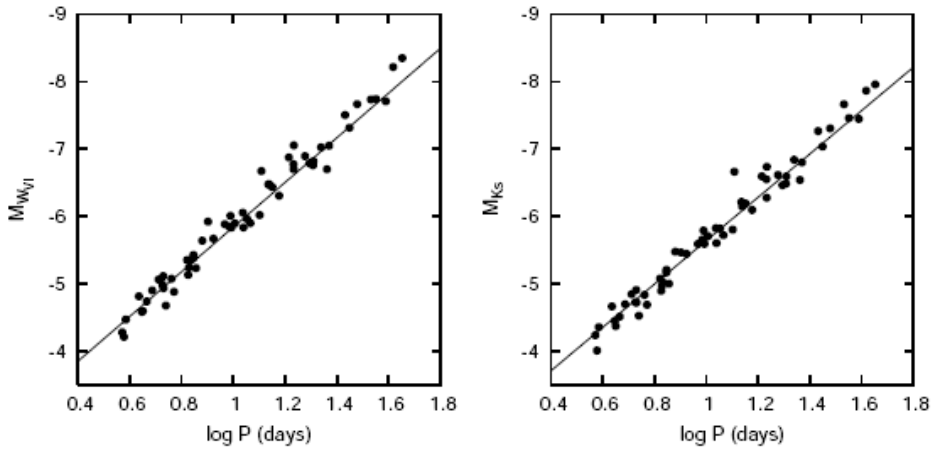

Fig. 4. Galactic *PL* relations in W_{VI} and K_s bands, superimposed with LMC Ogle relations shifted by a magnitude offset of 18.40.

Fig. 26.— Period – luminosity relations for Galactic Cepheids in V and in K bandpasses compared to that defined for Cepheids in the LMC using a mag. offset of 18.40. (Knowing the mean reddening of the LMC Cepheids, a distance to the LMC can thus be determined.) Fig. 4 of Fouque, Arriagada, Storm et al, 2007, A&A (in press) (see Astro-ph/0709.3255)

8. References and Suggested Reading

Textbooks:

Aerts, Christiansen-Dalsgaard, and Kurtz, Asterosismology

Christiansen-Dalsgaard – lecture notes, available on-line, see http:: users-phys.au.dk/jcd

Early key Kepler Papers on asteroseismology:

Chapiln, Basu, Huber et al, see arXiv:1310.4001

Hekker, Gilliland, Elsworth, 2011, MNRAS, 414, 2594 (see arXiv:103.0141)

Key references for early discoveries in the Sun include:

Leighton, Noyes & Simon, 1962, ApJ, 135, 474

Libbrecht, Woodard & Kaufman, 1990, ApJS, 74, 1134 (first detailed mode study)

Libbrecht & Woodard, 1991, Science, 253, 152 (overview as of 1991)